BENEMÉRITA UNIVERSIDAD AUTÓNOMA DE PUEBLA

INSTITUTO DE FÍSICA “LUIS RIVERA TERRAZAS”

“STUDY OF THE EFFECT OF OXYGEN VACANCY CONTENT ON THE PHOTOCATALYTIC ACTIVITY OF TiO_2 NANOPARTICLES”

TESIS

QUE PARA OBTENER EL GRADO DE

MAESTRA EN CIENCIAS
(EN LA ESPECIALIDAD DE CIENCIA DE MATERIALES)

PRESENTA
SELMA KURI HERNÁNDEZ

No. de CVU: 972755

DIRECTOR DE TESIS
DR. UMAPADA PAL

NOVIEMBRE DE 2021

In memory of Socorro Morales and Rosario Santamaría, who are always present in my mind and my heart, and inspire me to find the beauty in this life.

Dedicated to my parents Juan and Laura and to my brother Gibrán, for extending their love and support every moment, and for being my motivation to improve myself.

Acknowledgements

I would like to thank to my thesis advisor Dr. Umapada Pal for his constant supervision and guidance throughout the entire process of the thesis execution. I also want to thank my lab mates Francisco Cancino-Gordillo and Dr. José Luis Ortiz Quiñones for their continued support, understanding and for sharing their useful experiences in research with me, during this process.

I am grateful to the members of the evaluation committee: Dr. Siva Kumar Krishnan, Dra. María Eugenia Mendoza Álvarez and Dr. Gregorio Hernández Cocoletzi for the time dedicated in the revision and evaluation of the present work.

I would like to convey my deepest appreciation to my beloved parents for giving me the life, dedication for growing me up and help to achieve everything I wanted. My affectionate thanks go to my brother for his peculiar way of motivating me in every aspect of my life; to my boyfriend for his understanding, motivation and support during this process; and to my friends for their best wishes and encouragements for successful completion of this work.

I would like to thank Consejo Nacional de Ciencia y Tecnología (CONACyT), Mexico, for providing me the fellowship (CVU # 972755) and the financial help extended through the research project # CB 2017/2018-A1-S-26720 to carry out this research. I extend my sincere thanks to the Instituto de Física "Ing. Luis Rivera Terrazas" for giving me the opportunity to study the master degree.

Finally, I would like to Prof. Y.S. Kang, Sogang University, Seoul, and the members of his research group, for helping me to acquire the TEM images and XRD patterns of the TiO_2 nanostructures.

Content

Abstract

TiO_2 is one of the most popular metal oxide semiconductors utilized for advanced oxidation processes (AOPs), including in photocatalysis. As the photocatalytic behavior of a metal oxide is known to be controlled by oxygen vacancies (V_O), we prepared TiO_2 nanoparticles (NPs) of different V_O contents through thermally stimulated $NaBH_4$ reduction of commercial TiO_2 NPs Degussa P25, to study the effect of the degree of reduction (i.e., the concentration of V_O) on their photocatalytic performance, qualitatively. The reduced TiO_2 NPs were analyzed by X-ray diffraction (XRD), transmission electron microscopy (TEM), Raman spectroscopy, and diffuse reflectance spectroscopy (DRS) to understand the effect of $NaBH_4$ reduction on their structural and optical properties. N_2 adsorption-desorption isotherms of the samples were studied to analyze their texture parameters. Z-potential analysis was applied to estimate the surface potential of the nanostructures. The reduced and unreduced TiO_2 NPs were tested for photocatalytic degradation of methylene blue (MB), a model cationic organic dye. The results obtained in this study indicate that by increasing the amount of $NaBH_4$ in the reaction mixture, we can increase the V_O concentration in the nanostructures. While the incorporation of V_O enhances the photocatalytic activity of the metal oxide nanostructures, high concentration of V_O in the nanostructures induces higher adsorption of ionic dye molecules at their surfaces, blocking the passage of irradiated light and preventing the generation of enough e-h pairs, which effectively reduce their photodegradation performances.

Resumen

El TiO_2 es uno de los semiconductores de óxido metálico más populares empleados para los procesos de oxidación avanzados (AOP), incluido la fotocatálisis. Como ya es sabido, el comportamiento fotocatalítico de los óxidos metálicos está controlado por las vacancias de oxígeno (V_O), preparamos nanopartículas (NPs) de TiO_2 con diferentes concentraciones de V_O a través de la reducción por $NaBH_4$ estimulada térmicamente de las NPs comerciales de TiO_2 Degussa P25, para estudiar el efecto del grado de reducción (es decir, la concentración de V_O) en su desempeño fotocatalítico, de manera cualitativa. Las NPs de TiO_2 reducidas se analizaron mediante difracción de rayos X (XRD), microscopía electrónica de transmisión (TEM), espectroscopía Raman y espectroscopía de reflectancia difusa (DRS) para comprender el efecto de la reducción en sus propiedades estructurales y ópticas. Se estudiaron las isotermas de adsorción-desorción de N_2 de las muestras para analizar sus parámetros texturales. Se aplicó el análisis de potencial Z para estimar el potencial de superficie de las nanoestructuras. Las NPs de TiO_2 reducidas y no reducidas se analizaron para determinar la degradación fotocatalítica del azul de metileno (MB), un tinte orgánico catiónico modelo. Los resultados obtenidos en este estudio indican que al incrementar la cantidad de $NaBH_4$ en la mezcla de reacción, podemos incrementar la concentración de V_O en las nanoestructuras. Mientras que la incorporación de V_O mejora la actividad fotocatalítica de las nanoestructuras de óxidos metálicos, la alta concentración de V_O en las nanoestructuras induce una mayor adsorción de moléculas de colorante iónico en su superficie, bloqueando el paso de la luz irradiada, evitando la generación de suficientes pares de electrón-hueco, lo que efectivamente reduce su rendimiento en la fotodegradación de MB.

Chapter 1. Introduction

We have been told and taught for decades that the social and economic development involve human activities that influence negatively the environment and human health. In a more specific sense, the role played by textile industries in this context is crucial due to the large number of chemical pollutants, such as organic dyes that are released to aquatic environments.[1,2] One main drawback of these polluting dyes is their great resistance to biological, physical and chemical degradation methods. In order to solve this problem, the introduction and application of advanced oxidation processes (AOPs) is known as one of the most promising options. These AOPs involve the generation of oxidizing agents which are capable of degrading organic compounds, such as organic dyes.[3] Heterogeneous photocatalysis is an AOP, in which a semiconductor is used as a photocatalyst and is irradiated with light to generate electron-hole pairs, which has been extremely useful in the degradation of organic compounds.[4]

Titanium dioxide (TiO_2) based semiconducting materials have been studied for their application as photocatalysts. However, one of the most remarkable events that managed to focus the attention of several researchers working on TiO_2 for these applications occurred in 1972, when A. Fujishima and K. Honda demonstrated for the first time the photoelectrochemical decomposition of water using TiO_2 as an anode and platinum as the counter electrode.[5] Since then, TiO_2 has been one of the most studied semiconductors, with adequate physicochemical properties and good photocatalytic performance. However, the disadvantages of utilizing this semiconductor as a photocatalyst are its wide band gap energy and the rapid recombination of the photogenerated charge carriers (electrons and holes). Due to this, several methods have been tested to modify the surface of TiO_2, such as, doping with metals or non-metals and generation of oxygen vacancies (V_O) to improve the efficiency of its photocatalytic performance.[6-10]

To synthetize oxygen vacancy-rich metal oxides, several methods have been developed and applied. These methods are divided into two categories: post-treatment and in-situ manufacture. In the first category, a two-step process is required. In the first step the semiconducting metal oxide is synthetized. In the second step, a partial reduction on the

surface of the metal oxide is performed to remove O atoms and generate V_O. In contrast, in the in-situ manufacture method, V_O are generated during the synthesis of the metal oxide. The generation of V_O could be via nanocrystallization, solid transformation, low-valence metal doping, or light irradiation.[11]

The post-treatment methods are based on interfacial reactions and the solid-liquid reaction is one of them. Commonly, in this reaction, a reducing agent, such as polyalcohol, $NaBH_4$, or N_2H_4 is added to the solution containing a solvent and the metal oxide.[10] A practical and easy method for preparing partially reduced TiO_2 nanotubes is through $NaBH_4$ treatment, which has been reported to be effective in the production of V_O.[12]

Several studies suggested that the introduction of V_O or the formation of Ti^{3+} states at the surface of TiO_2 results in an upward displacement of the valence band maximum (VBM) and a downward displacement of the conduction band minimum (CBM), which enhances the capability of light absorption in the visible range and charge transport in TiO_2. These reported results indicate that modifying the surface of TiO_2 nanostructures through generation of V_O may contribute to the improvement of its photocatalytic efficiency.[13-15]

In this work, reduced TiO_2 nanoparticles were prepared following the chemical reduction method. Different samples of reduced nanoparticles were prepared, varying the amount of $NaBH_4$ for a fixed amount of TiO_2. Structural and morphological characterization were carried out employing the X-ray diffraction (XRD) and transmission electron microscopy (TEM) techniques. In order to analyze the effects of reduction on the optical properties of TiO_2 nanoparticles, UV-vis absorption spectroscopy in the diffuse reflectance (DRS) mode and Raman spectroscopy were carried out on the samples. N_2 adsorption-desorption isotherms of the samples were studied to analyze their texture parameters. Z-potential analysis was applied to estimate the surface potential of the nanostructures. Finally, the photocatalytic performance of the reduced nanoparticles was evaluated on the degradation of the organic dye methylene blue (MB) under UV and visible light irradiation.

References

1. Posthuma, L., Zijp, M., De Zwart, D., Van, D., Globevnik, L., Koprivsek, M., Focks, A., Gils, J., Birk, S. Chemical pollution imposes limitations to the ecological status of European surface waters. *Sci Rep* 10, 14825 (2020).

2. Jesudoss, N., Kumar, J., Kamyab, H., Sujana, J., Al-Khashman, O., Kuslu, Y., Ene, A., Kumar, B. Modern enabling techniques and adsorbents-based dye removal with sustainability concerns in textile industrial sector -A comprehensive review. *Journal of Cleaner Production* 272, 122636 (2020).

3. Tabar, M. B., Elahi, S. M., Ghoranneviss, M., Yousefi, R. The role of the Se-rich and Se-poor conditions in the photocatalytic performance of ZnSe/rGO nanocomposites. Applied Surface Science 523, 145819 (2020).

4. Paz, C.V., Ung, F., Zárate, J., Cortés, J.A. Evaluation of surface phenomena involved in photocatalytic degradation of Acid Blue 9 by TiO_2 catalysts of single and mixed phase – A theoretical and experimental study. *Applied Surface Science* 508, 145114 (2020).

5. Fujishima, A., Honda, K. Electrochemical Photolysis of Water at a Semiconductor Electrode. *Nature* 238, 37–38 (1972).

6. Al-Mamun, M. R., Kader, S., Islam, M. S., Khan, M. Z. H. Photocatalytic activity improvement and application of UV-TiO_2 photocatalysis in textile wastewater treatment: A review. *Journal of Environmental Chemical Engineering* 7, 103248 (2019).

7. Wu, Y., Xing, M., Zhang, J., Gel-hydrothermal synthesis of carbon and boron co-doped TiO_2 and evaluating its photocatalytic activity. *Journal of Hazardous Materials* 192, 368-373 (2011).

8. Bagwasi, S., Tian, B., Zhang, J., Nasir, M. Synthesis, characterization and application of bismuth and boron Co-doped TiO_2: A visible light active photocatalyst. *Chemical Engineering Journal* 217, 108-118 (2013).

9. Umebayashi, T., Yamaki, T., Simita, T., Yamamoto, S., Tanaka, S., Asai, K. UV-ray photoelectron and ab initio band calculation studies on electronic structures of Cr-or Nb-ion

implanted titanium dioxide. *Nuclear Instruments and Methods in Physics Research Section B: Beam Interactions with Materials and Atoms* 206, 264-267 (2003).

10. Swarnakar, P., Kanel, S. R., Nepal, D., Jiang, Y., Jia, H., Kerr, L., Goltz, N., Levy, J, Rakovan, J. Silver deposited titanium dioxide thin film for photocatalysis of organic compounds using natural light. *Solar Energy* 88, 242-249.

11. Huang, Y., Yu, Y., Yu, Y., Zhang, B. Oxygen Vacancy Engineering in Photocatalysis. Solar RRL 4, 8 (2020).

12. Kang, Q., Cao, J., Zhang, Y., Liu, L., Xu, J. Ye, J. Reduced TiO_2 nanotube arrays for photoelectrochemical water splitting. *Journal of Materials Chemistry A*, 1, 5766 (2013).

13. Zhu, S., Liang, S., Tong, Y., An, X., Long, J., Fu, X., Wang. X. Photocatalytic reduction of CO_2 with H_2O to CH_4 on Cu(I) supported TiO_2 nanosheets with defective {001} facets. *Physical Chemistry Chemical Physics* 17, 9761-9770 (2015).

14. Sorcar, S., Hwang, Y., Grimes, C. A. Highly enhanced and stable activity of defect-induced titania nanoparticles for solar light-driven CO_2 reduction into CH_4. *Materials Today* 20, 507-515 (2017).

15. Lin, Z., Orlov, A., Lambert, R., Payne, M. New Insights into the Origin of Visible Light Photocatalytic Activity of Nitrogen-Doped and Oxygen-Deficient Anatase TiO_2. *Journal of Physical Chemistry B* 109, 44, 20948–20952 (2005).

Chapter 2. Background

2.1 Titanium dioxide

Titanium dioxide (TiO_2), also known as titania, is a semiconducting material belongs to the groups IV-VI in the periodic table. It appears in three main polymorphs in nature: rutile, anatase and brookite.[1] In contrast to rutile and anatase phases which are easily available, brookite is hard to be found in nature. The fourth polymorph of TiO_2 occurring naturally is TiO_2(B), which is a bronze phase with a monoclinic structure. This mineral is still more rarely found than brookite and has been found exclusively in two geological locations.[2] Figure 2.1 shows the unit cell of each of the TiO_2 polymorphs. The four polymorphs are structured with TiO_6 octahedra, which consist of titanium (Ti^{4+}) atoms coordinated to six oxygen (O^{2-}) atoms. However, the difference among these types of TiO_2 relies on the distortion of the octahedron units, which share edges and corners in different ways. The structure of anatase is made up of corner sharing octahedra, forming (001) planes, which results in a tetragonal structure (Fig. 2.1a). In rutile, the octahedra share edges at (001) planes, resulting also in a tetragonal structure. In brookite, the octahedra share both corners and edges to form an orthorhombic structure. Finally, the TiO_2(B) phase consists of folded sheets with octahedra sharing both corners and edges.[3-4]

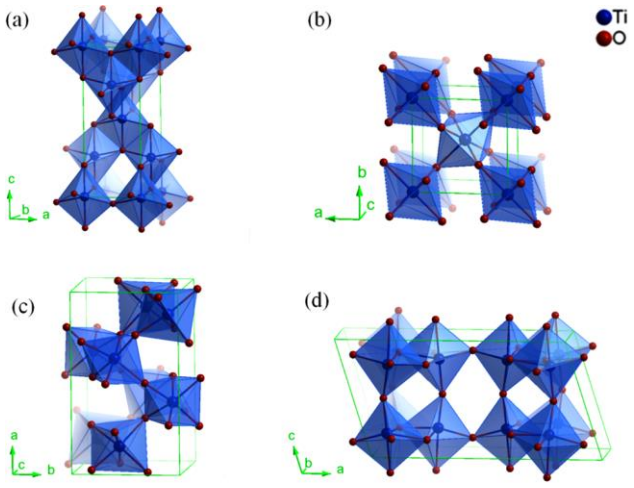

Figure 2.1. Schematic unit cells of crystal structures of TiO_2 in its different polymorphs: (a) anatase, (b) rutile, (c) brookite and (d) TiO_2(B).[3]

Rutile is known to be the most thermodynamically stable phase; whereas anatase, brookite and TiO_2(B) are considered to be metastable. However, rutile can be obtained by annealing any of the other three polymorphs at high temperatures.[3,6]

Due to the oxygen vacancies, TiO_2 is an n-type semiconductor.[5] Titanium dioxide is a wide bandgap semiconductor. The bandgap for rutile phase is 3.03 eV, and 3.2 eV for anatase. However, there is limited information about the bandgap energy of the other phases. The reported band gap energy of brookite vary in-between 3.1 and 3.4 eV.[2] Although TiO_2 occurs in the mentioned polymorphs, it is more common to find it in the anatase and rutile phases. The most important properties of these two phases are summarized in Table 2.1.[6]

Property	Anatase	Rutile
Crystal structure	Tetragonal	Tetragonal
Atoms per unit cell (Z)	4	2
Space group	$I4_1/amd$	$P4_2/mnm$
Lattice parameters (nm)	a = 0.3785 c = 0.9514	a = 0.4594 c = 0.2959
Unit cell volumen (nm^3)	0.1363	0.0624
Densty ($kg\ m^{-3}$)	3894	4250
Calculated indirect band gap		
(eV)	3.23-3.59	3.02-3.24
(nm)	345.4-383.9	382.7-410.1
Experimental band gap		
(eV)	~3.2	~3.0
(nm)	~387	~413
Refractive index	2.54, 2.49	2.79, 2.903

Table 2.1. Main properties of anatase and rutile.[6]

Due to some characteristics of TiO_2 such as low cost, high photostability, high UV light absorption, biological and chemical stability, this semiconductor has been one of the most widely investigated and applied as a photocatalyist.[7-10]

2.2 Photocatalytic mechanism in TiO_2

Previously, we have mentioned that TiO_2 is a semiconductor, but we have not defined what a semiconductor is. A semiconductor is a material whose electrical conductivity lies in-between that of a conductor and an insulator. The electrical conductivity of a semiconductor is defined by its band structure, which is composed of the valence band (VB) and the conduction band (CB). The interaction of the highest occupied molecular orbital (HOMO) constitutes the VB, while the CB is defined by the lowest unoccupied molecular orbital (LUMO).[11] In TiO_2, the valence band is composed of O 2p orbitals and the conduction band is composed of the Ti 3d, 4s and 4p orbitals.[12] The energy between the CB and the VB is known as bandgap or energy gap, denoted as E_g.

In a typical photocatalytic reaction (utilizing TiO_2 as photocatalyst), the semiconductor is irradiated with photons of energy equal to or greater than its E_g. The photons are absorbed generating electron-hole pairs. The electron in the VB will be transferred to the CB, leaving a hole in its place. The following equation represents this reaction:

$$TiO_2 + h\nu \rightarrow h^+ + e^-$$

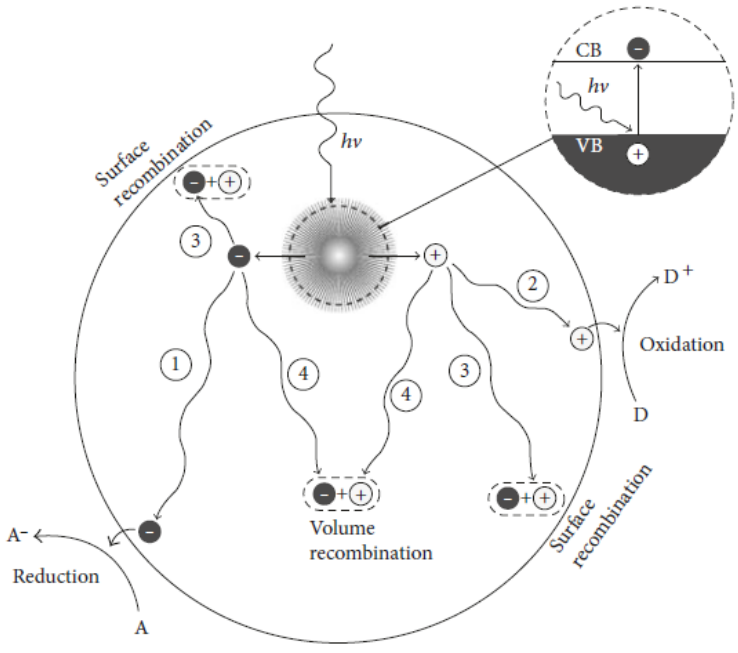

Figure 2.2. Schematic demonstration of the photocatalytic mechanism of TiO_2 with two types of recombination. A is electron acceptor, and D is electron donor.[13]

These photogenerated charge carriers (electrons and holes) are responsible for the redox reactions useful for the mineralization of toxic compounds, but they can be recombined, decreasing the chances of reaching to the CB. Therefore, the recombination process involves a reduction of the overall efficiency of the photocatalytic process (see Figure 2.2). On the other hand, electrons and holes that do not recombine, can migrate to the surface of TiO_2 and participate in redox reactions with surface adsorbed molecules. For example, the electrons, e^- in the CB, participates in a reduction reaction, because it can react with molecular oxygen (O_2) to form superoxide radicals $\cdot O_2^-$, or hyperoxide radicals $HO_2\cdot$.

$$O_2 + e^- \rightarrow \cdot O_2^-$$

Also, the holes (h^+) in the VB participate in oxidation reactions either with surface adsorbed hydroxides or with water, producing hydroxyl radicals ·OH.[14] (See Figure 2.3).

$$H_2O + h^+ \rightarrow \cdot OH + H^+$$

The radicals $\cdot O_2^-$, $HO_2\cdot$ and ·OH are commonly known as reactive oxygen species (ROS), and they are responsible for the degradation of organic compounds. In a photocatalytic process, the photodegradation efficiency strongly depends on the type of semiconductor used and on the properties of organic pollutants.[15-16]

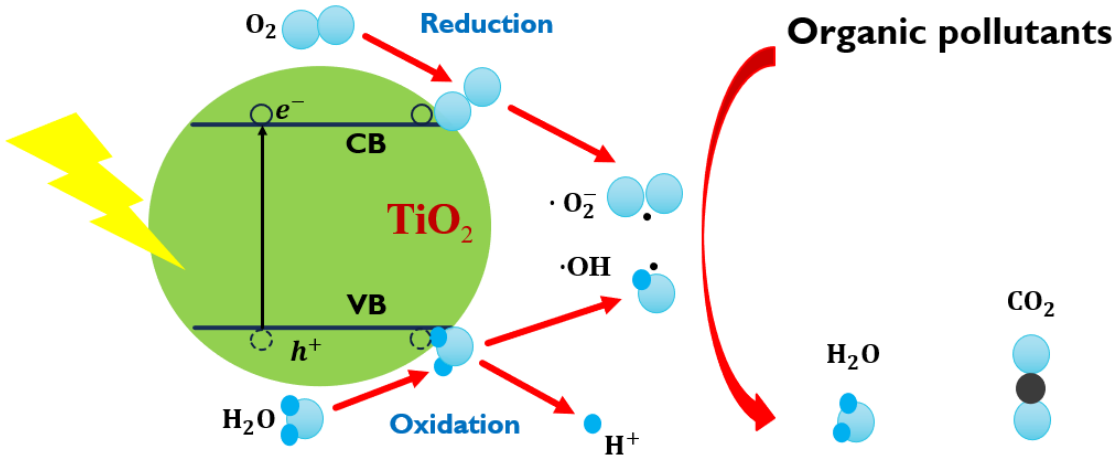

Figure 2.3. Involved redox reactions taking place on TiO_2 surface during photocatalysis.[14]

One important aspect is that the photocatalytic activities of TiO_2 in anatase and rutile phases are different. As can be seen in Table 2.1, different crystal structures of the semiconductor generate different electronic band structures (and consequently a difference in their bandgap energies) and different mass densities. Due to these differences, anatase shows a better photocatalytic performance than rutile, even though its bandgap is wider. This difference has been attributed to the higher density of localized states in anatase, which implies that charge carrier recombination is slower and causes a slightly higher redox driving force than in rutile.[3,6] Moreover, the surface area of anatase is much larger than rutile, which improves the adsorption capability and enhances the generation of active sites, for instance, oxygen vacancies.

Previously, we mentioned that TiO_2 is the most studied photocatalyst, but it is very common to use commercial TiO_2, such as Degussa P25. This is a powder constituted by both anatase and rutile phases. It is reported that a mixture of these two polymorphs shows a better photocatalytic activity than pure phases. This is due to a band alignment between these phases, which favors the transfer of photogenerated electrons from anatase to rutile, and the transfer of holes from rutile to anatase at a clean interface.[18] Within this synergistic effect, also occurs that the lower band gap of the rutile nanocrystals creates energy wells that trap electrons and prevent electron-hole recombination.[19]

2.3 Disadvantages of TiO_2 as a photocatalyst

Despite of that TiO_2 is the most used photocatalyst, there are some disadvantages of its application. These disadvantages are: the rapid recombination of photogenerated electron-holes, which reduces the quantum efficiency; and the high bandgap energy, which limits light absorption to the UV region only (wavelengths less than 390 nm). Therefore, there are limitations in using this semiconductor for photocatalytic applications in the visible spectral range of light.[13]

2.4 Improvements on photocatalytic activity of TiO_2

In order to improve the photocatalytic activity of TiO_2, a huge effort has been devoted to extend its light absorption to the visible region. The strategies developed can be summarized as: (i) bandgap engineering, which refers to narrowing the bandgap of TiO_2 by introducing other elements into this semiconductor or using a special preparation method; and (ii) surface

sensitization, which refers to the application of other visible light active materials as a light harvester to sensitize TiO_2.[3] In this work, we focus only on the first strategy.

2.5 Bandgap engineering of TiO_2

Withing this category we can find the following strategies to reduce the bandgap energy of TiO_2:

2.5.1 Doping with cations

When TiO_2 is doped with other cations replacing Ti^{4+}, an impurity level will be introduced in its forbidden band. As a result, this intermediate energy level can act either as an electron acceptor or an electron donor, which contributes to the light absorption of TiO_2 in the visible spectra range. In addition, cation doping usually leads to quite localized d states, deep into the bandgap of TiO_2, acting as recombination centers for charge carriers. In 1982 Bogarello et al. reported the photocatalytic H_2O splitting reaction on Cr^{3+} doped TiO_2 nanoparticles under visible light. The visible light absorption was attributed to the photoexcited transition of Cr^{3+} 3d electrons into the CB of TiO_2.[20]

It was also found that co-doping with two cations exhibits higher activity than single cation doping. For example, Niishiro et al. found that Ni^{2+} doped TiO_2 can produce H_2 from aqueous methanol solution under visible light irradiation. However, when they co-doped with Nb^{5+}, the absorption intensity of TiO_2 increased in the visible region. Moreover, this is a reason why co-doping of two cations with different charges may increase the stability of the photocatalyst due to a charge balancing effect.[21]

It is important to mention that not all the improvements in the photocatalytic activity are due to the visible light absorption of cation-doped TiO_2. For instance, a significantly enhanced photocatalytic activity of rare earth doped TiO_2 for H_2 production has been associated to the improvement of the particle dispersion and the increase of surface area.[22]

2.5.2 Doping with anions

Another strategy to enhance the light absorption of TiO_2 in visible spectral range is anion doping. In contrast to cation doping, anion doping can affect the CB of this semiconductor,

which is constituted of Ti 3d, 4s y 4p orbitals. It can usually reconstruct the VB and shift it upward to narrow the bandgap.

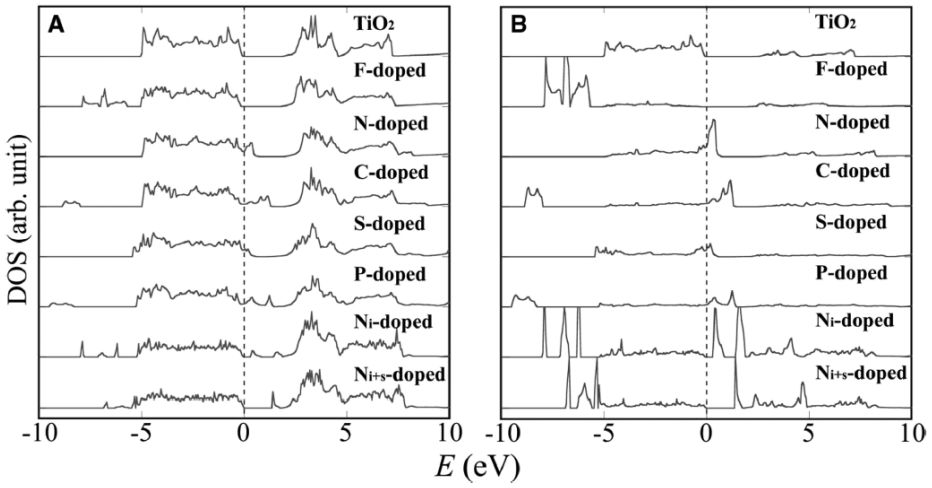

Figure 2.4. Total densities of states of doped TiO_2 (A) and the projected densities of states into the doped anions sites (B), calculated by FLAPW (full-potential linearized augmented plane wave).[23]

The densities of states of some anions including C, N, F, P, or S substituting O in anatase TiO_2 are shown in Figure 2.4. It is noticeable that N is the most suitable doping element because its p orbitals contribute to the VB by mixing with O 2p orbitals, which can narrow the bandgap of TiO_2 by shifting the VB upward.[23] However, it is also believed that N doping may introduce local states and oxygen vacancies inside de bandgap and this gives place to the extension of light absorption in the visible region rather than a bandgap narrowing.[24]

On the other hand, C and P are two elements that also can introduce some midgap-states, but the problem is that these states are not well overlapped with the band states of TiO_2. On the other hand, S, having a large ionic radius is technologically hard to be doped into TiO_2, but it could generate a smaller bandgap. Some results of X-ray photoelectron spectroscopy (XPS) had revealed that S, C or N doping may create some additional electronic states above the VB edge of TiO_2, which gives rise to a red shift of band edge energy of these anion-doped TiO_2.[25]

It has also been observed that TiO_2 co-doped with two anions shows higher photocatalytic activity than single anion-doped TiO_2. For instance, Luo et al. investigated Cl and Br co-

doped TiO_2 and they found that the absorption edge of the co-doped TiO_2 shifted to a lower energy region, which leads to a higher activity in H_2 prouction.[26]

2.5.3 Co-doping with cations and anions

We can also extend the visible light absorption of TiO_2 by co-doping with both anions and cations. For example, Gai and co-workers found that co-doping with charge-compensated donor-acceptor pairs, such as C and Mo, can remarkably rise the edge of the VB of TiO_2 while the CB keeps almost unchanged.[27]

We must take into account that the effect of doping may create catalytic active sites, which could promote either the oxidation of reagents or the reduction of protons, improving the overall photocatalytic activity.[3]

2.5.4 Doping free visible light responsive TiO_2

Due to some disadvantages of ion-doped TiO_2 such as instability and the possibility of acting as recombination centers and decreasing the photocatalytic activity,[28] doping free TiO_2 with visible light response has been the object of study in recent years.[29]

In 2009, Sasikala and co-workers utilized sonochemical, polyl and solvothermal methods to synthesize self (Ti^{3+}) doped TiO_2 and they found that all of the samples showed the onset of absorption at ~440 nm, which was attributed to the defect levels that originated from the oxygen vacancies.[30] Also, Zuo et al. developed a combustion method to synthesize TiO_{2-x}, which exhibited a high stability in air and water under light irradiation. Through electron paramagnetic resonance (EPR) spectroscopy of the materials, they found that the presence of Ti^{3+} in the bulk, was responsible for the visible light absorption.[31] Later, Xing et al. developed a solvothermal method to prepare self-doped (Ti^{3+}) TiO_2 with $NaBH_4$ as a reductant. They considered the oxygen vacancies were responsible for the Ti 3d defect states in the forbidden band.[32] However, based on the result of high-resolution scanning tunneling microscopy and photoelectron spectroscopy measurements, Wandt and co-workers proposed that Ti interstitials in the near-surface region generate the defect state in the bandgap, which is responsible for the visible light absorption of titania.[33]

2.5.5 The role of oxygen vacancies in TiO_2

Generally, with the introduction of oxygen vacancies (V_O) in metal oxides, changes occur in their atomic and electronic structures. Consequently, aspects such as charge generation, separation and surface reactions can be modified or modulated. The role of oxygen vacancies is divided into three processes: photon absorption, charge-carrier separation and surface reaction.[34] Each one of them will be explained in detail below.

(a) Extend light absorption range. As we mentioned earlier, when a semiconductor is irradiated, photons with energy higher than the bandgap will be absorbed, generating electron-hole pairs. If the bandgap of a semiconductor such as titania is narrowed down, its range of light absorption will be extended. In this context, when an oxygen atom is removed from the lattice, the excess of electrons generated is transferred and injected into the 3d orbitals of the adjacent metal atoms (Ti). This will result in the formation of shallow level below the conduction band minimum (CBM). Moreover, it has been demonstrated that the increase in V_O causes the rise of these shallow levels and may even overlap the bandgap.[35] On the other hand, metal ions can also donate electrons to the oxygen ions surrounding the defective site, resulting in the formation of a level above the valence band maximum (VBM), which will narrow the bandgap.[36]

Figure 2.5 (a) shows the surface facet (101) of TiO_2 anatase. It also schematically represents the density of states, the CB and VB, which are composed of Ti 3d and O 2p orbitals, respectively. In Fig. 2.5 (b), we can appreciate that the formation of V_O on anatase (101) results in an excess of surface electrons in the form of localized Ti^{3+} ions (marked in yellow), which are also known as polarons. The corresponding defect states have energies within the bandgap, which leads to light absorption in the visible region. It could also improve the reactivity towards various adsorbates. Finally in Fig. 2.5 (c), there is a higher concentration of V_O at the surface of TiO_2 nanoparticles, which leads to the formation of black TiO_2. This black TiO_2 contains so many defects that it is capable of absorbing almost all the visible light.[37]

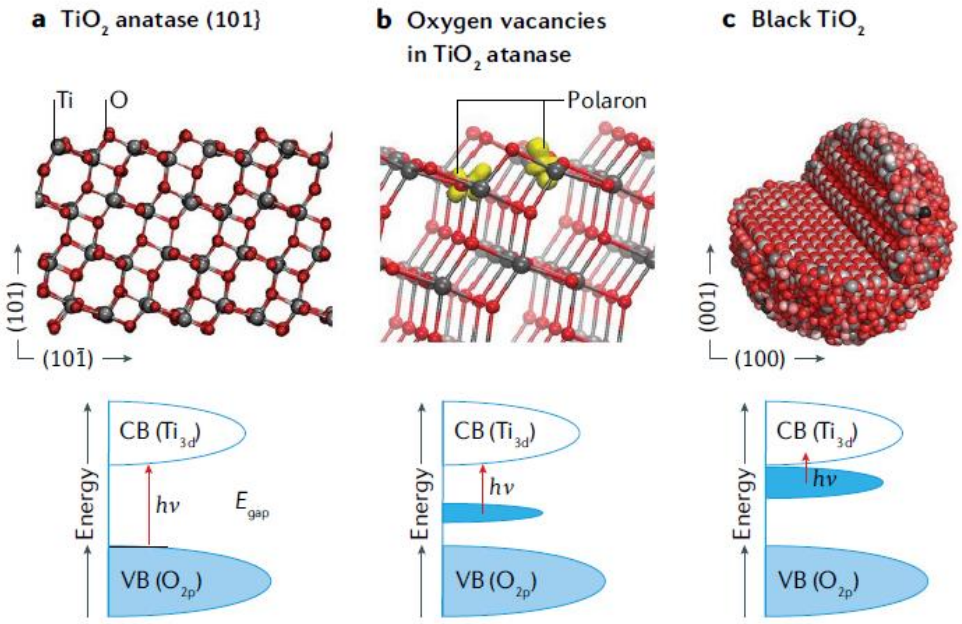

Figure 2.5. Changes in the TiO_2 light absorption due to the influence of V_O.[37]

(b) Promote charge-carrier separation. When an electron-hole pair is generated in the semiconductor due to light irradiation, there will be a "competition" between the recombination of photoinduced charge carriers and the charge-carriers transfer. Usually, the photogenerated electrons in the CB easily return to the VB and recombine with the photogenerated holes.[38] However, as has been stated earlier, generation of V_O can narrow the bandgap and increase the conductivity of the semiconductor. In addition, V_O on the surface of titania can serve as reactive sites and trap the separated charge carriers for subsequent surface reactions. This is how there is less opportunity for the electron-hole pairs to meet and recombine. However, the concentration and distribution of oxygen vacancies must be carefully designed and constructed to promote the performances of the semiconductor photocatalyst.[34]

(c) Improve surface reaction. The photocatalytic reactions take place at surface-active sites. However, the intrinsic atomic structure and electronic structure of active sites are critical to the catalytic activity and selectivity. Therefore, oxygen vacancies not only create active sites with different coordination numbers and dangling bonds, but also increase the local electron density. For example, Li and co-workers demonstrated that the surface V_O on TiO_2

nanosheets can effectively stabilize Au single atoms through the formation of Ti-Au-Ti bond, which could reduce the energy barrier and promote the catalytic properties.[39] Also, Xu et al. developed a defect-mediated reduction process to prepare a series of V_O-rich TiO_2-supported noble metal nanoparticles, using Ag, Pt and Pd, with outstanding photocatalytic performances.[40]

References

1. Haggerty, J.E.S., Schelhas, L.T., Kitchaev, D.A. et al. High-fraction brookite films from amorphous precursors. *Scientific Reports*, 7, 15232 (2017).

2. Kalyanasundaram, K. (2010) Dye-Sensitized Solar Cells. EPFL Press, Lausanne. pp. 45-47.

3. Ma, Y., Wang, X., Jia, Y., Chen, X., Han, H. and Li, C. Titanium Dioxide-Based Nanomaterials for Photocatalytic Fuel Generations. *Chemical Reviews,* 114, 9987-10043, (2014).

4. Pelaez, M., Nolan, N., Pillai, S., et al. A review on the visible light active titanium dioxide photocatalysts for environmental applications. *Applied Catalysis B: Environmental*, 125, 331-349 (2012).

5. Wisitsoraat, A., Tuantranont, A., Comini, E., Sberveglieri, G., and Wlodarski, W. Characterization of n-type and p-type semiconductor gas sensors bases on NiO_x doped TiO_2 thin films. *Thin Solid Films*, 517, 2775-2780 (2009).

6. Hanaor, D., and Sorrell, C. Review of the anatase to rutile phase transformation. *Journal of Materials Science*, 46 (4), 855-874 (2011).

7. Han, F., Mao, X. & Xu, Q. Flower-like Au/Ag/TiO_2 nanocomposites with enhanced photocatalytic efficiency under visible light irradiation. *Science China Chemistry* 60, 521–527 (2017).

8. Okuno, T., Kawamura, G., Muto, H. *et al*. Three modes of high-efficient photocatalysis using composites of TiO_2-nanocrystallite-containing mesoporous SiO_2 and Au nanoparticles. *Journal of Sol-Gel Science and Technololgy*, 74, 748–755 (2015).

9. Guohong, L., Houng, L., Hongshi, Z., *et al*. Chemical assembly of TiO_2 and TiO_2@Ag nanoparticles on silk fiber to produce multifunctional fabrics. *Journal of Colloid and Interface Science*, 358, 307-315 (2011).

10. Spivey, J., Dooley, K. M. (2009) Catalysis. *The Royal Society of Chemistry*. SPR-Catalysis, volume 21.

11. Yu, P., Cardona, M. (2010) Fundamentals of Semiconductors. Physics and Materials Properties. Springer.

12. Xu, A. W., Gao, Y., Liu, H. Q. The Preparation, Characterization, and their Photocatalytic Activities of Rare-Earth-Doped TiO_2 Nanoparticles. *Journal of Catalysis,* 207, 151 (2002).

13. Yan, X., Li, Y., and Xia, T. Black Titanium Dioxide Nanomaterials in Photocatalysis. International Journal of Photoenergy, Vol. 2017 |Article ID 8529851.

14. Banerjee, S., Pillai, S., *et al*. New Insights into the Mechanism of Visible Light Photocatalysis. *Journal of Physical Chemistry Letters* 5, 15, 2543-2554 (2014).

15. Paz, C.V., Ung, F., Zárate, J., Cortés, J.A. Evaluation of surface phenomena involved in photocatalytic degradation of Acid Blue 9 by TiO_2 catalysts of single and mixed phase – A theoretical and experimental study. *Applied Surface Science* 508, 145114 (2020).

16. Nosaka, Y., and Nosaka A. Y. Generation and Detection of Reactive Oxygen Species in Photocatalysis. *Chemical Reviews* 117, 11302−11336 (2017).

17. Luttrell, T., Halpegamage, S., Tao, H., Kramer, A., Sutter, E., and Batzill, M. Why is anatase a better photocatalyst than rutile? - Model studies on epitaxial TiO_2 films. *Scientific Reports* 4, 4043 (2014).

18. Scanlon, D., Dunnill, C., Buckeridge, J., et al. Band alignment of rutile and anatase TiO_2. *Nature Materials* 12, 789-801 (2013).

19. Bouras, P., Sthatos, E., and Lianos, P. Pure versus metal-ion-doped nanocrystalline titania for photocatalysis. Applied Catalysis B: Environmental, 73, 51-59 (2007).

20. Dholam, R., Patel, N., and Miotello, A. Hydrogen production by photocatalytic water-splitting using Cr- or Fe-doped TiO_2 composite thin films photocatalyst. *International Journal of Hydrogen Energy* 34, 5337-5346 (2009).

21. Niishiro, R., Kato, H. and Kudo, A. Nickel and either tantalum or niobium-codoped TiO_2 and $SrTiO_3$ photocatalysts with visible-light response for H_2 or O_2 evolution from aqueous solutions. *Physical Chemistry Chemical Physics,* 10, 2241 (2005).

22. Matsumoto, Y., Kurimoto, J., Shimizu, T., Sato, E. Photoelectrochemical properties of polycrystalline TiO_2 doped with 3d transition metals. *Journal of the Electrochemistry Society* 128, 1040 (1981).

23. Asahi, R., Morikawa, T., Ohwaki, T., Aoki, K., Taga, Y. Visible-light photocatalysis in nitrogen-doped titanium oxides. *Science* 293, 269 (2001).

24. Wang, J., Tafen, D., Lewis, P.; Hong, L., Manivannan, A., Zhi, M., Li, M., Wu, J. Origin of Photocatalytic Activity of Nitrogen-Doped TiO_2 Nanobelts. *American Chemical Society* 131, 34 12290-12297 (2009).

25. Chen, X. B., Burda, C. The Electronic Origin of the Visible-Light Absorption Properties of C-, N- and S-Doped TiO_2 Nanomaterials. *Journal of the American Chemical Society*, 130, 5018 (2008).

26. Luo, H., Takata, T., Lee, Y., Zhao, J., Domen, K., Yan, Y. Photocatalytic Activity Enhancing for Titanium Dioxide by Co-doping with Bromine and Chlorine. *Chemistry of Materials* 16, 846 (2004).

27. Gai, Y., Li, J., Li, S., Xia, J., Wei, S. Design of Narrow-Gap TiO_2: A Passivated Codoping Approach for Enhanced Photoelectrochemical Activity. *Physical Review Letters* 102, 036402 (2009).

28. Choi, W., Termin, A., and Hoffmann, M. Effects of Metal-Ion Dopants on the Photocatalytic Reactivity of Quantum-Sized TiO_2 Particles. *Journal of Physical Chemistry* 98, 13669 (1994).

29. Liu, X., Gao, S., Xu, H., Lou, Z., Wang, W., Huang, B., Dai, Y. Green synthetic approach for Ti^{3+} self-doped TiO_{2-x} nanoparticles with efficient visible light photocatalytic activity. *Nanoscale* 5, 1870 (2013).

30. Sasikala, R., Sudarsan, V., Sudakar, C., Naik, R., Panicker, L., Bharadwaj, S. Highly dispersed phase of SnO_2 on TiO_2 nanoparticles synthesized by polyol-mediated route: photocatalytic activity for hydrogen generation. *International Journal of Hydrogen Energy* 34, 6105 (2009).

31. Zuo, F., Wang, L., Wu, T., Zhang, Z., Borchardt, D., Feng, P. *Journal of American Chemical Society* 132, 11856 (2010).

32. Xing, M., Fang, W., Nasir, M., Ma, Y., Zhang, J., Anpo, M. Self-doped Ti^{3+}-enhanced TiO_2 nanoparticles with a high-performance photocatalysis. *Journal of Catalysis* 297, 236 (2013).

33. Wendt, S., Sprunger, P., Lira, E., Madsen, G., Li, Z., Hansen, J., Matthiesen, J., Blekinge-Rasmussen, A., Laegsgaard, E., Hammer, B., Besenbacher, F. The role of interstitial sites in the Ti3d defect state in the band gap of titania. *Science* 320, 1755 (2008).

34. Huang, Y., Yu, Y., Yu, Y., Zhang, B. Oxygen Vacancy Engineering in Photocatalysis. *Solar RRL* 4, 8 (2020).

35. Pan, X., Yang, M., Fu, X., Zhang, N., and Xu, Y. Defective TiO_2 with oxygen vacancies: synthesis, properties and photocatalytic applications. *Nanoscale*, 5, 3601 (2013).

36. Naldoni, A., Altomare, M., Zoppellaro, G., Liu, N., Kment, S., Zboril, R., and Schmuki, P. Photocatalysis with Reduced TiO_2: From Black TiO_2 to Cocatalyst-Free Hydrogen Production. *ACS Catalysis* 9, 345 (2019).

37. Glezakou, V.-A., and Rousseau, R. Shedding light on black titania. *Nature Materials* 17, 856–857 (2018).

38. Xu, L., Zhao, H., Sun, M., et al. Cover Picture: Oxygen Vacancies on Layered Niobic Acid That Weaken the Catalytic Conversion of Polysulfides in Lithium–Sulfur Batteries. *German Chemical Society* 58, 11127 (2019).

39. Wan, J., Chen, W., Jia, C., et al. Defect Effects on TiO_2 Nanosheets: Stabilizing Single Atomic Site Au and Promoting Catalytic Properties. *Advanced Materials* 30, 1705369 (2018)

40. Pan, X., and Xu, Y-J. Efficient Thermal- and Photocatalyst of Pd Nanoparticles on TiO2 Achieved by an Oxygen Vacancies Promoted Synthesis Strategy. *ACS Applied Materials and Interfaces* 6, 3 (2014).

Chapter 3. Materials preparation and used characterization techniques

3.1 Preparation of reduced TiO_2 nanoparticles

As has been mentioned earlier (in chapter **1**), several methods have been utilized by the researchers for producing vacancy-rich metal oxides, which can be divided into two categories: post-treatment and in-situ manufacturing.[1] The post-treatment methods are based on interfacial reactions and the solid-liquid reaction is one of them. Commonly, in these reactions, a reducing agent, such as polyalcohol, $NaBH_4$, N_2H_4, etc., is added to the solution containing a solvent and the metal oxide.[2] On the other hand, in in-situ manufacturing process, the metal oxide nanostructures are grown under reducing ambient.

In the present study, we utilized the earlier (post-treatment) method for preparing reduced TiO_2 from the commercial TiO_2 nanoparticles. The procedure adapted to prepare the TiO_2 nanoparticles reduced at different extents is based on the work reported by Sorcar et al.,[3] with some modifications as described below:

First, the commercial TiO_2, Degussa P25 (Rutile/Anatase: 30:70, purity: 99.9%) of a certain amount (~ 1 g) was mixed with different amounts of sodium borohydride ($NaBH_4$, Alfa Aesar, 98%). The TiO_2 powder and $NaBH_4$ were ground in an Agata mortar for a few minutes to obtain a homogeneous mixture of the compounds. The obtained mixture was transferred to an alumina crucible and placed inside the quartz tube of a horizontal furnace (Carbolite). The oxygen inside the sealed quartz tube was removed by Ar flow for 30 min (200 sccm). Then the sample inside the quartz tube was then heated at 350° C (at 20° C/min heating rate) for 30 min under Ar gas flow. After thermal treatment, the samples were washed with abundant deionized water and ethanol (several times). The samples were dried in a vacuum oven at 90 °C for 12 h. Different samples of reduced TiO_2 were prepared by varying the amount of $NaBH_4$. The samples were labeled as DG-Y, where Y corresponds to the quantity of $NaBH_4$ in wt %. Following the process, we prepared 4 samples and designated them as DG-0, DG-10, DG-15 and DG-25. The prepared samples are shown in Figure 3.1.

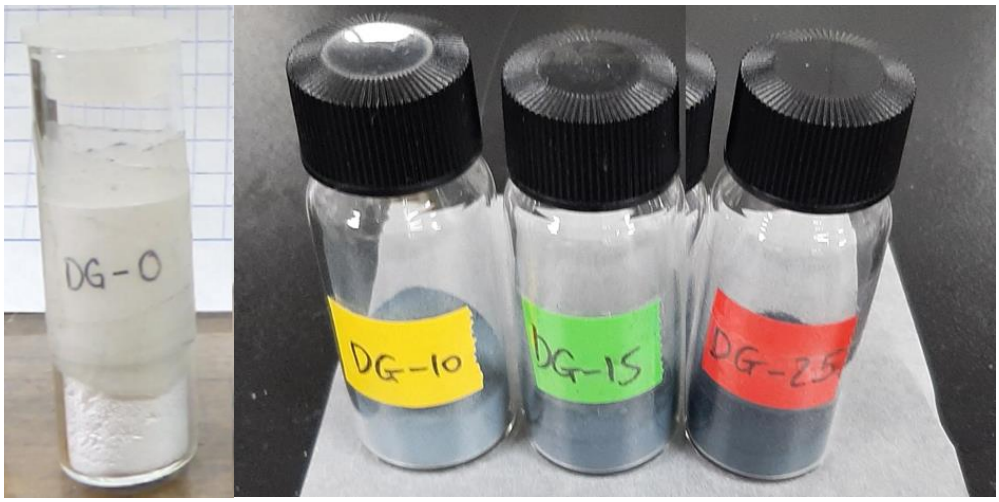

Figure 3.1. Prepared samples of the reduced and unreduced TiO_2 nanoparticles. The darkening in the color indicates the generation of oxygen vacancies at the surface of nanoparticles.

3.2 Characterization techniques

In this section, we describe all the techniques utilized for characterizing the TiO_2 nanoparticles and testing their photocatalytic activities.

3.2.1 X-ray Powder Diffraction

X-ray powder diffraction (XRD) is one of the most efficient, non-destructive characterization techniques, which is mainly used for phase identification of crystalline materials and extracting information on their unit cell and other structural parameters.

In 1895 the German physicist Roentgen discovered X-rays and he named them that way because their nature was not understood at that time. However, people empirically knew that X-rays were invisible light, travelling in straight lines and capable of affecting photographic films, just as visible light does. They also found that X-rays could penetrate deeper into a material than visible light and, consequently, pass through the human body, thick pieces of metal, wood and some opaque materials. With this in mind, physicians and engineers started to use them in the development of radiography, primarily used for medical purposes.

After some years, it became clear that X-rays are electromagnetic radiation, whose typical photon energies are in the range of 100 eV and 100 keV. They can be generated by either synchrotron radiation or X-ray tubes. Generally, X-ray tubes are used as the primary X-ray sources in laboratory equipments. In X-ray tubes, a high voltage difference is applied between the anode and the cathode. The electrons coming from the tungsten filament (cathode) are accelerated and allowed to collide on the metallic target (anode). After the collision of such high energy electrons with target atoms, they slow down and a continuous spectrum of X-rays is emitted. This is an ionization process, in which the electrons with high energy eject the inner shell electrons of the target atoms.

There are two types of X-ray spectra that can be obtained when the accelerated electrons from the filament reach the metallic target:

- Continuous spectra. They consist of a range of X-ray wavelengths with minimum wavelength and intensity depending on the metal target and the voltage across the X-ray tube. With increasing voltage, the wavelength decreases and the intensity increases.

- Characteristic spectra. They are produced at high voltages as a result of specific electronic transitions, which take place in the individual atoms of the metallic target. Each one of these transitions produces an X-ray photon with a wavelength that depends on the structure of the irradiated atom. A transition from the L shell to the K shell produces a K_α X-ray, while the transition from the M shell to the K shell produces a K_β X-ray (see Figure 3.2). These characteristics X-rays have higher intensities than those produced in the continuous spectra, with $I_{K\alpha} > I_{K\beta}$. The wavelengths of these characteristic X-rays are different for the different atoms in the periodic table.

In powder XRD, as the name suggests, usually a sample in powder form is used. The sample usually consists of fine grains of single crystalline material, although it could be also a liquid suspension or a polycrystalline solid.

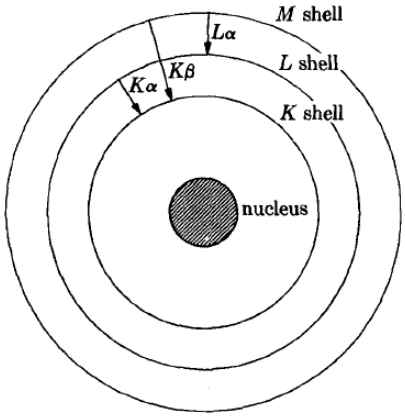

Figure 3.2. Schematic representation of the electronic transitions in an atom. The emission process is indicated by arrows.[4]

The X-ray diffraction process has its basis in the phenomenon of wave interference. When incident rays in a crystalline sample are scattered in all directions, they can produce both constructive and destructive interference phenomena, depending on the phase difference. When the phase difference is nλ, (where λ is the wavelength and n is the order number), constructive interference occurs and a phase difference of nλ/2, destructive interference occurs. The X-rays that collide on a crystalline solid will be diffracted by crystallographic planes as illustrated in Figure 3.3. We can observe two incident electromagnetic waves being deflected by two interatomic planes. These deflected waves will be in phase only if the following relationship is satisfied:

$$n\lambda = 2d\ \sin\theta \tag{3.1}$$

where d is the interplanar spacing of the crystalline solid and θ is the incident angle. This is the well-known Bragg´s law of diffraction and it establishes that the path difference of two propagating X-ray beams is dependent on the incident angle θ, and the distance between two interatomic planes d. For both the diffracted beams to be in phase, the path difference must be equal to:[4]

$$CB + BD = 2d\ \sin\theta = n\lambda \tag{3.2}$$

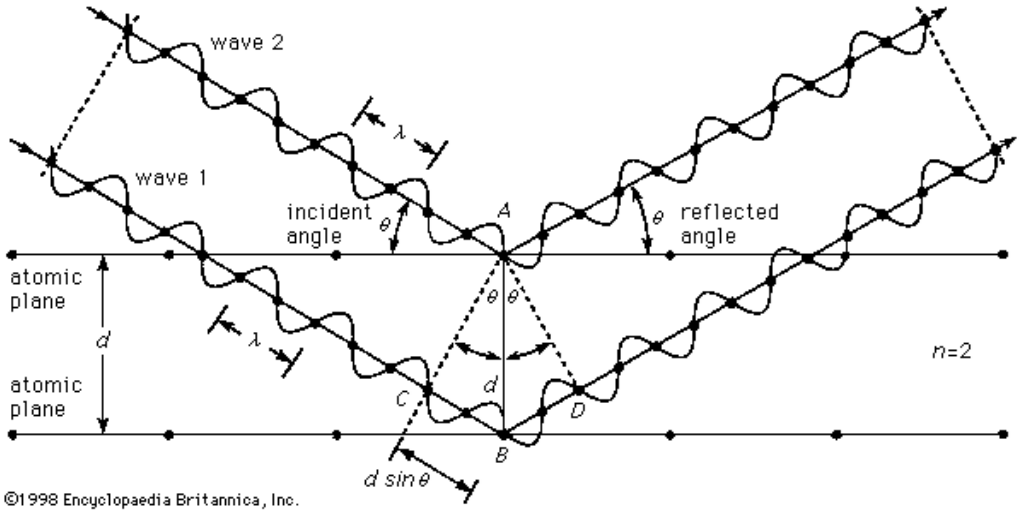

Figure 3.3. Diffraction of X-rays by a crystal.[5]

The diffractometer is the instrument utilized to examine crystalline samples. Once the sample is analyzed, it is possible to obtain a graphic pattern (diffractogram) of the variation of intensity of the diffracted X-rays in function of the θ angle or 2θ. Using the Bragg´s law, we can obtain the value of d for each diffraction peak corresponding to the 2θ angle. In this way, it is possible to identify the crystalline structure of the sample, associating each diffraction peak to different interatomic planes in terms of the Miller indices (hkl), and comparing the spectrum with a known database (PDF file) for the particular material.

The structural characterization of the nanoparticles (unreduced and reduced TiO_2 nanoparticles) under investigation was carried out in a Bruker D8-Discover diffractometer (at the Artificial Photosynthesis Center, Department of Chemistry, Sogang University, South Korea) with monochromatic K_α emission of Cu (λ=1.5406 Å) at room temperature, in a 2θ range of 20-80°, at a scan rate of 1º/min at 0.014º per step.

3.2.2 Transmission Electron Microscopy (TEM)

Transmission electron microscopy (TEM) is a very useful characterization technique, which allows us to analyze certain aspects of materials such as their crystallinity and other structural features such as defects and grain orientations. The technique is also useful for analyzing the

growth of layers, as well as their composition and defects. Additionally, the high-resolution transmission (HRTEM) allows to study the quality, shape and size of individual crystallites.

After the discovery of the wave-like behavior of electrons, Louis de Broglie proposed that the wavelength of the electron is given by $\lambda = h/p = h/(mv)$, where h is the Planck constant, and p, m and v are the momentum, mass and speed of the electron, respectively. Later, it was observed that the wavelength of electrons emitted into vacuum and being accelerated through a potential difference of 50 kV is about 5 pm. As a result, these high-energy electrons were capable of penetrating several micrometers of depth into a solid. When the solid is crystalline, the electrons will be diffracted by atomic planes inside the material, just like in the case of X-ray diffraction phenomenon; but in this case, a transmitted electron diffraction pattern is formed when the electrons pass across a thin sample. Then, it was discovered that when the transmitted electrons are focused, their short wavelength would let the sample to be scanned with a better spatial resolution than that of a light-optical microscope. In addition to the wave-like behavior, the focusing of electrons is based on the fact that they act as negatively charged particles and, for this reason, they are deflected by electric and magnetic fields.[6]

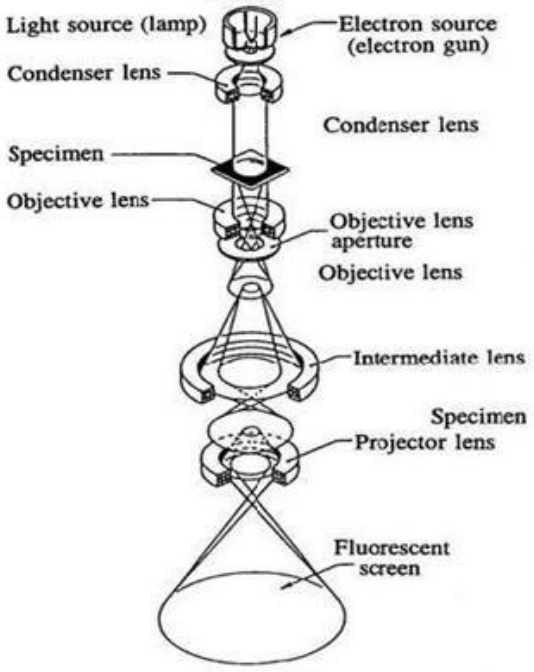

Figure 3.4. Schematic illustration of different components of a Transmission electron microscope (Taken from JEOL 2000FX Handbook).

A schematic representation of a transmission electron microscope is shown in Figure 3.4. The beam of electrons coming from the electron source (electron gun) is focused into a thin and coherent beam with the aid of the condenser lenses. The condenser aperture restricts the width of the beam and excludes the high angle electrons. Then, the selected beam shines on the sample (specimen) and, depending on the thickness of the specimen, parts of the beam can be transmitted. Subsequently, the transmitted beam is focused by the objective lens into an image on a charge coupled device (CCD) camera. Thus, after the image projected had passed down the column across the intermediate and projector lenses, it is amplified. The image strikes the fluorescent screen and generates light, which allows the user to visualize the image.

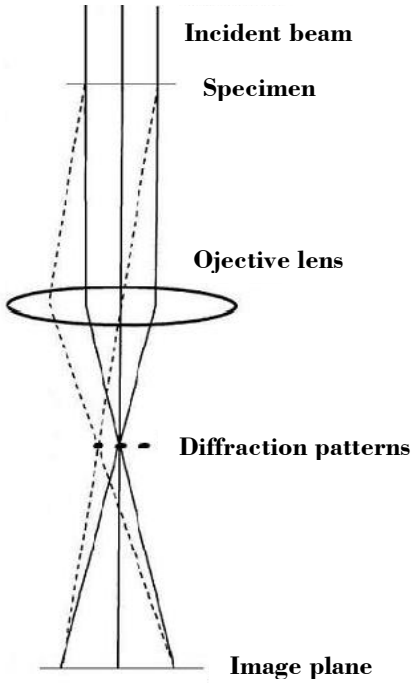

Figure 3.5. Schematic representation of the diffraction mechanism in TEM.[7]

Figure 3.5 shows the path of the beam of electrons in a transmission electronic microscope, above the specimen and down the column to the fluorescent screen in Figure 3. The electrons

that pass through the specimen are scattered by the electrostatic potential, which is set up by the constituent element in the sample. Once, they have passed across the sample, they pass through the electromagnetic objective lens which focuses the scattered electrons from one point of the sample into one point on the image plane.

On visualizing the image, the darker parts of it represent those areas in the sample that fewer electrons were transmitted across. On the other hand, the brighter areas represent those parts in the sample where more electrons were transmitted across.[7] In order to evaluate the morphology and size of the nanoparticles prepared in the present investigation, a Jeol JEM 2100F transmission electron microscope (TEM, at the Artificial Photosynthesis Center, Department of Chemistry, Sogang University, South Korea) operating at 200 kV was utilized.

3.2.3 Diffuse Reflectance Spectroscopy (DRS)

Diffuse reflectance spectroscopy (DRS), which also called as diffuse reflection spectroscopy, belongs to the category of absorption spectroscopy. DRS is a non-invasive, non-destructive characterization technique, which is commonly used to obtain optical spectra of powders with minimum sample preparation. Generally, a reflectance spectrum is obtained from the analysis of surface-reflected electromagnetic radiation as a function of the frequency or the wavelength. This spectrum gives information about the optical properties of the measured sample.

Usually, there can occur two types of reflection: specular reflection, which is associated with reflection from polished or smooth surfaces, such as mirrors; and diffuse reflection, which is associated with the reflection from mat or opaque surfaces textured like powders. Both are schematically illustrated in Figure 3.6.

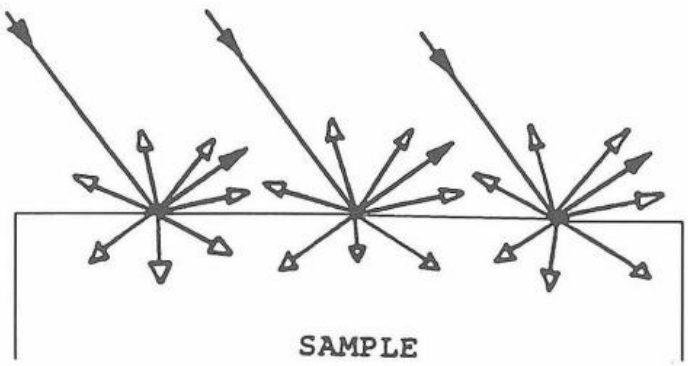

Figure 3.6. Specular reflection, denoted by the solid arrows, is radiation whose angle of reflection equals the angle of incidence. Diffuse reflection, denoted by hollow arrows, is radiation whose angle of reflection is independent of the angle of incidence.[8]

Diffuse reflectance can be explained as follows: first, let us consider a white wall illuminated by sunlight. We can observe that the wall looks equally bright, no matter if we stand directly in front of it, or at any other angle. The surface of the wall reflects the incident sunlight at angles independent of the angle of incidence. This means that the surface of the wall scatters the incoming radiation in all directions. A requirement for the ideal diffuse reflectance is that the angular distribution of the reflected radiation be independent of the angle of incidence.[8]

The most often utilized theory to describe and analyze diffuse reflectance spectra is the theory developed by Kubelka and Munk.[9] It was originally proposed to describe the behavior of light traveling inside a light-scattering specimen, which is based on these differential equations:

$$-\mathrm{di} = -(\mathrm{S} + \mathrm{K})\mathrm{idx} + \mathrm{Sjdx} \tag{3.3}$$

$$\mathrm{dj} = -(\mathrm{S} + \mathrm{K})\mathrm{jdx} + \mathrm{Sidx} \tag{3.4}$$

where i and j are the intensities of light traveling inside the sample towards its un-illuminated and illuminated surfaces, respectively; dx is the differential segment along the light path; and S and K are the K-M scattering and absorption coefficients, respectively.

In the liming case of an infinitely thick sample, the influence of the thickness and sample holder can be neglected and the Kubelka-Munk equation at any wavelength reads:

$$\frac{K}{S} = \frac{(1 - R_\infty)^2}{2R_\infty} \equiv F(R_\infty) \tag{3.5}$$

$F(R_\infty)$ is known as the remission function, and $R_\infty = R_{sample}/R_{standard}$.

Considering the parabolic band structure of an indirect band gap semiconductor, it is well known that the band gap E_g, and the absorption coefficient α are related through the equation:

$$ahv = C_1\left(hv - E_g\right)^2 \tag{3.6}$$

where α is the linear absorption coefficient of the sample, hv is the photon energy and C_1 is a proportionality constant. If the material scatters in a perfectly diffuse manner, the K-M absorption coefficient K becomes equal to 2α. In this case, we can consider that the K-M scattering coefficient S is constant with respect to wavelength, and using the remission function, we obtain:

$$[F(R_\infty)hv]^{1/2} = C_2\left(hv - E_g\right) \tag{3.7}$$

In this way, we can plot $[F(R_\infty)hv]^{1/2}$ as a function of hv to obtain the band gap E_g of a powder sample.[10] In this work, diffuse reflectance spectroscopy was applied to determine the band gap energy of the nanostructures. A Carry-5000 spectrophotometer (Varian, at the Central Laboratory, IFUAP) with diffuse reflectance accessory (integrating sphere DRA-CA-30I) attachment was utilized to characterize the powder samples.

3.2.4 Raman Spectroscopy

Raman spectroscopy belongs to the category of vibrational spectroscopy, where light is used to excite molecular vibration in a material. This characterization technique is commonly used in different scientific fields; for instance, in biology it is possible to study protein conformations and water binding properties; in solid state physics, it allows to obtain information about particular phonon modes; and in chemistry it is useful to identify molecules through structural informations.

When light interacts with matter, its electromagnetic field perturbs the charge distribution in the matter, leading to an exchange of energy and momentum and leaving the matter in a modified state. More specifically, when an incident photon interacts with a crystal lattice or

molecule, there can occur two types of scattering: the elastic and the inelastic one. Elastic scattering is more predominant in light, it happens when the energy of the scattered photon is equal to that of the incident photon. This type of scattering is known as Rayleigh scattering. On the other hand, inelastic scattering of light occurs when the energy of the scattered photon is not equal to that of the incident photon, and this is known as Raman effect. This last process gives rise to a modified state in the molecule.

If the energy of the scattered photon is lower than that of the incident photon, the process is referred as Stokes Raman scattering. In contrast, when the energy of the scattered photon is higher than that of the incident photon, the process is referred as anti-Stokes Raman scattering, (see Figure 3.7). This scattering phenomenon was predicted by Adolf Smekal in 1923 and discovered by C.V. Raman in 1930.

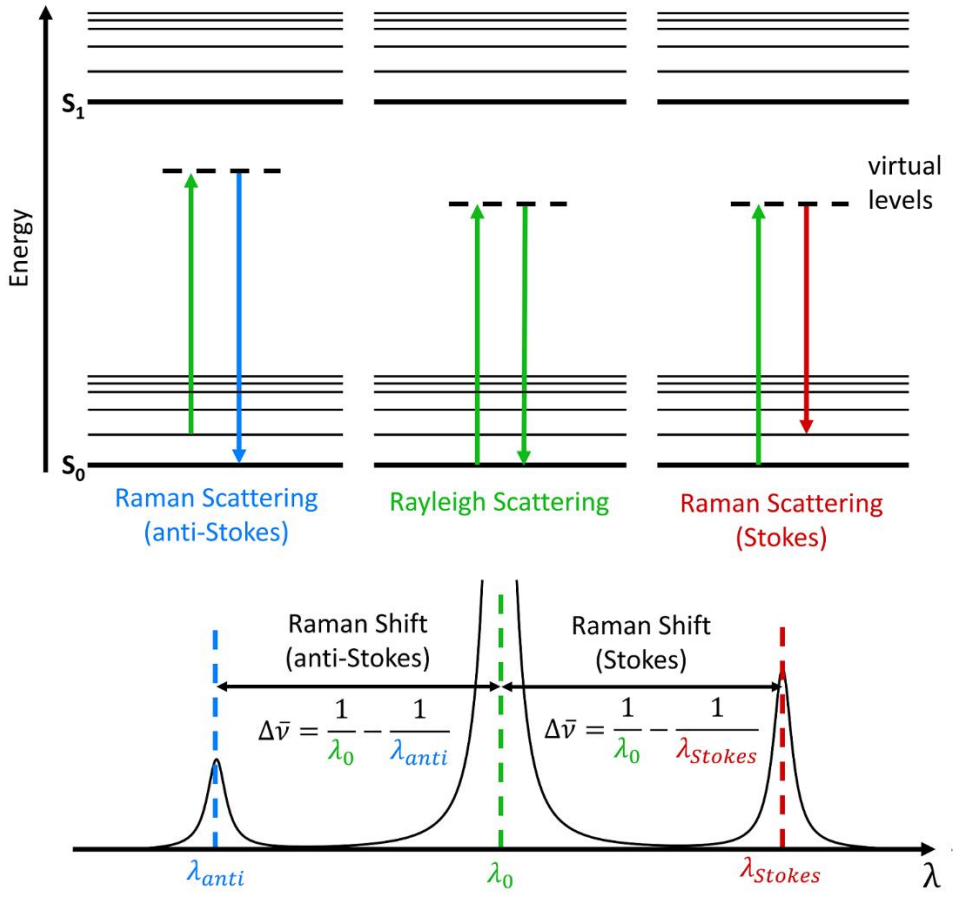

Figure 3.7. Schematic representation of Rayleigh, Stokes and anti-Stokes scattering and their origins.

In a Raman spectroscopy system (spectrometer), the laser must be focused onto the sample of interest. However, it is important that the sample does not show fluorescence to the laser utilized for excitation, because the Raman effect is weaker in comparison to fluorescence.[11]

Once the sample has been irradiated by the laser, the scattered light is transferred through a filter, in order to exclude (discard) any signal (photon) coming from the excitation laser. After that, the light is directed to a grating, to distribute the inelastic parts like a prism and according to the wavelength. Finally, the obtained beam is directed to a CCD (Charge Coupled Device) sensor, which generates a spectrum, i.e., intensity in function of Raman shift.

In this work, the nanoparticles were characterized at room temperature, using a Raman Horiba Lab RAM HR spectrometer (at the Central Laboratory, IFUAP) with a He-Ne (633nm) laser as the excitation laser and a thermoelectrically cooled CCD camera.

3.2.5 BET Surface area determination

The Brunauer, Emmett and Teller (BET) theory[12] has been commonly used to evaluate and explain the physical adsorption of gas molecules on a solid surface. The result of the specific surface area is generated from the gas adsorption data. The BET theory can be applied to systems of multilayer adsorption and it is very common to use probing gases that do not chemically interact or react with the material which plays the role of the adsorbent surfaces and, in this way, to make a quantitative characterization of the surface area. For this reason, nitrogen (N) is the most commonly used gas in BET surface area measurements, and this is why a standard BET analysis is carried out at the boiling temperature of N_2 (77 K).

Adsorption can be defined as the enrichment of molecules, atoms or ions in the vicinity of an interface. In the case of gas or solid systems, adsorption takes place in the vicinity of the solid surface and outside the solid structure. Adsorption can be physical or chemical. Physisorption is the physical adsorption that occurs whenever an adsorbable gas is brought into contact with the surface of a solid. The intermolecular forces involved are of the same kind as those responsible for the imperfection of real gases and the condensation of vapors. In addition to the attractive dispersion forces and the short-range repulsive forces, specific molecular

interactions usually occur as a result of particular geometric and electronic properties of the adsorbent. On the other hand, in chemisorption, which is the chemical adsorption, the intermolecular forces involved lead to the formation of chemical bonds.[13]

The application of the BET method involves two stages. First, it is necessary to transform physisorption isotherm into a "BET plot" (described in the following sentences), and from it to derive a value of the BET monolayer adsorbed quantity, v_m. The second stage consist to calculate the BET-area from v_m by adopting a suitable value of the molecular cross-sectional area. The BET equation is given by:

$$\frac{{}^{p}/_{p_0}}{v_a\left(1-{}^{p}/_{p_0}\right)} = \frac{1}{v_m C} + \frac{C-1}{v_m C}\left(\frac{p}{p_0}\right) \qquad (3.8),$$

where v_a is the specific amount of adsorbed gas at the relative pressure ${}^{p}/_{p_0}$ (p and p_0 are the equilibrium and the saturation pressure of the adsorbates at the temperature of adsorption), and C is the BET constant.[13] The equation (3.8) corresponds to an adsorption isotherm and can be plotted as a straight line with $1/v_a\left[\left({}^{p}/_{p_0}\right)-1\right]$ as a function of ${}^{p}/_{p_0}$, which is well known as the BET plot. With this plot it is possible to estimate the values of C and v_m and, therefore, to calculate the total and the specific surface area.

In this work, the determination of the specific surface area of the samples was carried out from their nitrogen adsorption-desorption isotherms at 77 K recorded in a Belsorp-Mini II (BEL Japan, Inc.) analyzer (at the Nanostructure laboratory, IFUAP).

3.2.6 Z-potential measurement

The Z-potential is a characterization technique, which measures the magnitude of electrostatic repulsion or attraction between particles, and is one of the fundamental parameters known to affect the stability of a materials, especially in nanoscale. Measurement of Z-potential provides detailed information on the causes of dispersion or aggregation, and can be applied to improve the formulation of dispersions, emulsions and suspensions.

In an ionic solution, nanoparticles with a net charge have a layer of ions strongly bound to their surface. A second diffuse outer layer is comprised of loosely associated ions. These two layers are collectively called the electrical double layer. As the particle moves, a distinction is created between ions in the diffuse layer that move with the nanoparticle and ions that remain with the bulk dispersant. The electrostatic potential at this "slipping plane" boundary is called the Z-potential and is related to the surface charge of the nanoparticle. In Z-potential measurements, an electrical field is applied across the sample and the movement of the nanoparticles, which is known as electrophoretic mobility, is measured by laser doppler velocimetry (LDV). The equation used to calculate the Z-potential, Z, is the Henry's equation:

$$U_e = \frac{2\,\varepsilon z\, f(\kappa a)}{3\eta} \qquad (3.9),$$

where U_e is the electrophoretic mobility, ε is the dielectric constant, η is the absolute zero-shear viscosity of the medium, $f(\kappa a)$ is the Henry function, which is a measure of the ratio of the particle radius to the Debye length. Nanoparticles with a Z-potential between -10 and +10 mV are considered approximately neutral, while nanoparticles with Z-potentials of greater that +30 mV or less than -30 mV are considered strongly cationic and anionic, respectively.[14] The parameters required for determining Z-potential are: refractive index, liquid dielectric constant, and viscosity. This makes Z-potential measurement to be a technique rapid and reliable.

In this work, the Z-potential measurements of the samples were carried out in a Zetasizer Nano (Malvern Panalytical) at 25°C (at the Central Laboratory, Ecocampus, IFUAP), with a prior control of the pH of the dispersing medium (water).

3.2.7 Photocatalytic evaluation of TiO_2 and reduced TiO_2 nanoparticles

The photocatalytic evaluation of the pristine and reduced TiO_2 nanoparticles was carried out in aqueous solutions inside a cylindrical glass reactor of 200 mL capacity. For this purpose, the organic dye, methylene blue (MB) ($C_{16}H_{18}ClN_3S \cdot 3H_2O$, Sigma-Aldrich) was used as a model pollutant dye to evaluate the photocatalytic activity of the samples. The catalytic

reaction mixtures were prepared adding 30 mg of the photocatalyst (pristine/reduced TiO_2 nanoparticles) in 60 mL dye solution (MB, 10 ppm). The aqueous solutions were mixed under magnetic stirring for 10 minutes in a glass reactor in the dark.

In order to monitor the degradation process of MB, first the absorption spectra of the solutions with catalyst particles in the dark were recorded every 10 minutes. Once the adsorption-desorption equilibrium is reached (i.e., there is no variation in the absorption intensity), a 10 W ultraviolet LED lamp (model JX-10UV9XIB365) with emission wavelength $\lambda = 365$ nm, was placed on the top of the glass reactor. The temperature of the reaction mixture was kept almost constant at about 18° C by circulating cold water through the jacket of the glass reactor. A reusable syringe with nitrocellulose membrane filter of 0.22 μm pore size was used to separate the dispersed photocatalyst from the aliquots (3.5 mL volume) before measuring their absorption spectra. The concentrations of MB in the reaction solution were estimated from the absorption spectra recorded at different time intervals, using a pre-calibrated concentration curve. The concentration of the analyte was obtained by monitoring the change in intensity of the major absorption band of MB located around 664 nm. The photocatalytic evaluation was carried out in the Nanostructure laboratory, IFUAP.

References

1. Huang, Y., Yu, Y., Yu, Y., Zhang, B. Oxygen Vacancy Engineering in Photocatalysis. Solar RRL 4, 8 (2020).

2. Swarnakar, P., Kanel, S. R., Nepal, D., Jiang, Y., Jia, H., Kerr, L., Goltz, N., Levy, J, Rakovan, J. Silver deposited titanium dioxide thin film for photocatalysis of organic compounds using natural light. *Solar Energy* 88, 242-249.

3. Sorcar, S., Hwang, Y., Grimes, C. A. Highly enhanced and stable activity of defect-induced titania nanoparticles for solar light-driven CO_2 reduction into CH_4. *Materials Today* 20, 507-515 (2017).

4. B. D. Cullity, S. R. Stock. (1978). Elements of X-Ray diffraction. Second edition. Addison-Wisley.

5. Augustyn, A., Zelazko, A., et al. "Britannica". https://www.britannica.com/science/Bragg-law. [Access October 2021]

6. Egerton, R. F. (2016). Physical Principles of Electron Microscopy, An Introduction to TEM, SEM, and AEM. Second edition. Springer.

7. Williams, D., Carter, C. (2009). Transmission Electron Microscopy, A Textbook for Materials Science. Second edition. Springer.

8. Blitz, P. J. (1998). Modern Techniques in Applied Molecular Spectroscopy. John Wiley & Sons, Inc.

9. Kubelka, P., and Munk, F. Ein Beitrag Zur Optik Der Farbanstriche. *Techn. Phys.*, 12, 593 -601 (1931).

10. Morales, A. E., Sánchez, E., Pal, U. Use of diffuse reflectance spectroscopy for optical characterization of un-supported nanostructures. *Revista Mexicana de Física* S 53 (5) 18–22 (2006).

11. Jones, R., Hooper, D., Zhang, L., Wolverson, D., and Valev, V. Raman Techniques: Fundamentals and Frontiers. *Nanoscale Research Letters* 14, 231 (2019).

12. Brunauer, Stephen; Emmett, P. H.; Teller, Edward. Adsorption of Gases in Multimolecular Layers. *Journal of the American Chemical Society* 60 (2): 309-31 (1938).

13. Thommes, M., Kaneki, K., Neimark, A., Olivier, J., Rodríguez-Reinoso, F., Rouquerol, J., Sing, K. Physisorption of gases, with special reference to the evaluation of surface area and pore size distribution (IUPAC Technical Report). Pure and Applied Chemistry 87, 9-10 (2015).

14. Clogston J. D., Patri A. K. (2011) Zeta Potential Measurement. In: McNeil S. (eds) Characterization of Nanoparticles Intended for Drug Delivery. Methods in Molecular Biology (Methods and Protocols), vol 697. Humana Press.

Chapter 4. Results and discussion

X-ray diffraction (XRD) patterns of the samples were recorded at room temperature to estimate the lattice parameters and structural defects in the nanostructures.

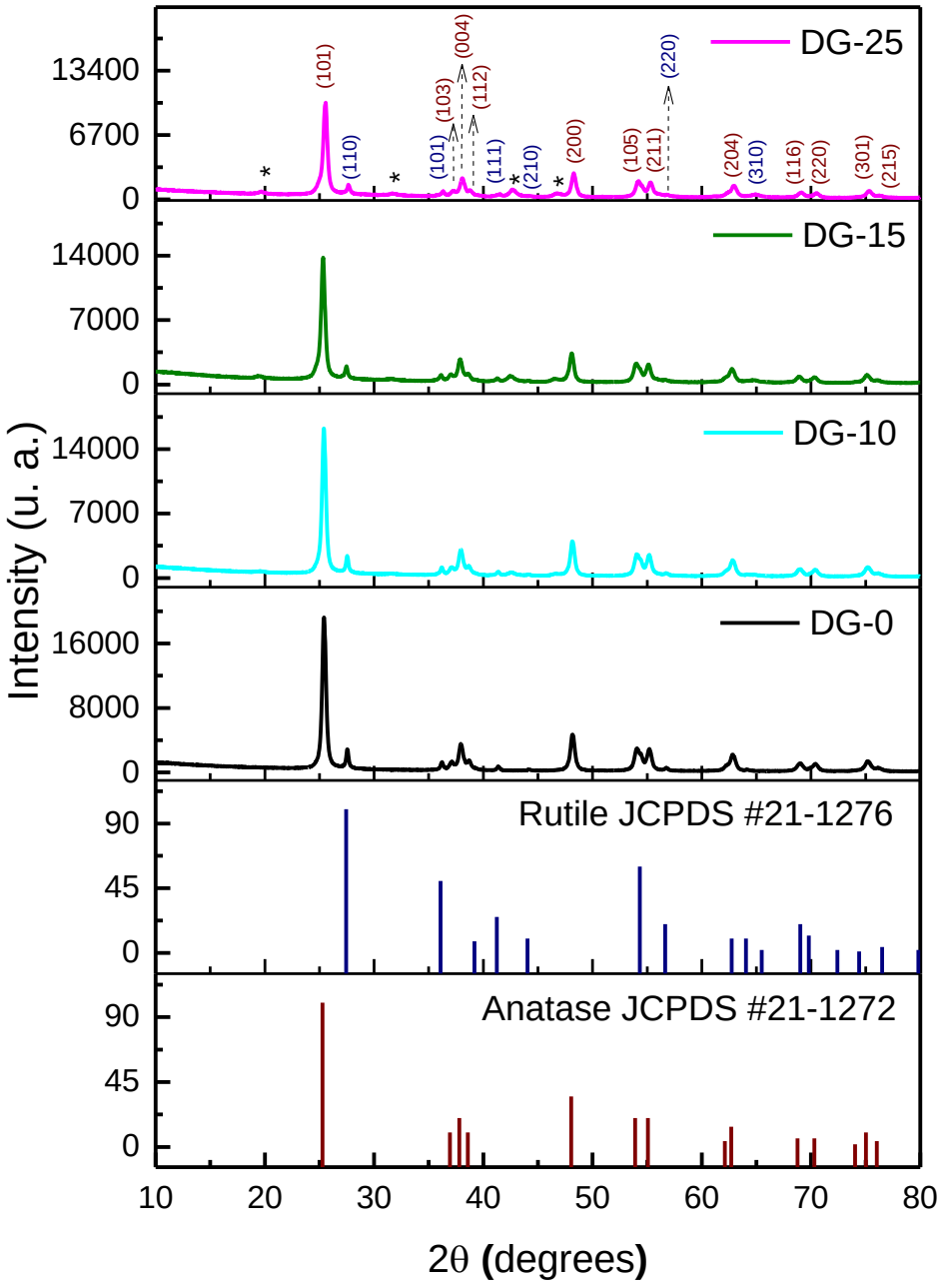

Figure 4.1. XRD patterns of the pristine and reduced TiO_2 nanoparticles prepared with different amounts of $NaBH_4$. The patterns were smoothened with 4-point averaging. The unidentified diffraction peaks (of very low intensity) are marked by asterisks.

The XRD patterns of the reduced and unreduced TiO_2 sample are presented in Figure 4.1. All the samples revealed well defined diffraction peaks correspond to their mixed (anatase and rutile) structural phases, indicating their good crystallinity. The resolved diffraction peaks correspond to anatase (JCPDS Card no. 21-1272) and rutile (JCPDS Card no. 21-1276) phase are indexed according to their standard diffraction data files. As can be noticed in Figure 4.1, the $NaBH_4$-reduced samples revealed some additional diffraction peaks at 19.56, 31.57, 42.54 and 46. 61°, marked with black asterisks, which were not present in the XRD pattern of the unreduced (pristine) TiO_2 (Degussa P25) sample.

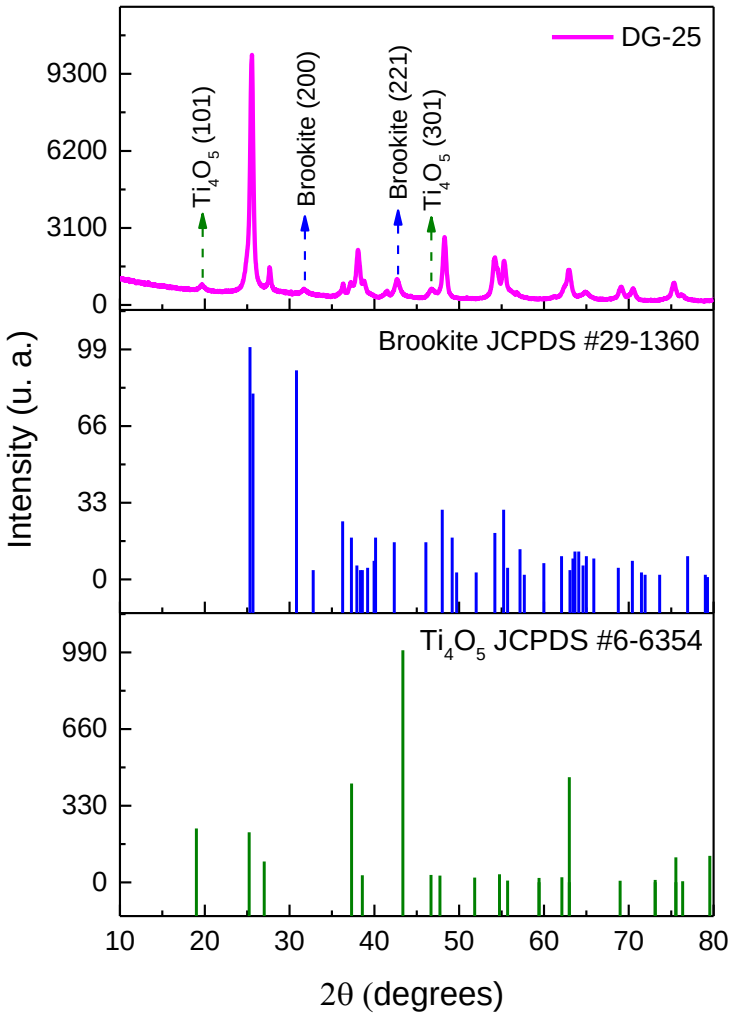

Figure 4.2. XRD patterns of the DG-25 sample.

Appearance of such additional diffraction peaks in the XRD patterns of $NaBH_4$-reduced TiO_2 has also been reported by Sorcar et al.,[1] and Ye et al.[2] While Sorcar et al. did not assign those peaks to any undesired phase or sub-oxide of TiO_2, Ye et al. assigned them to sub-oxides of TiO_2, such as Ti_4O_5 (JCPDS Card no. 06-6354) and $TiO_{0.89}$, produced during the reduction of TiO_2 by $NaBH_4$. It was also found that some of these additional peaks correspond to TiO_2 in brookite phase (JCPDS Card no. 29-1360). These new peaks are indicated in Figure 4.2, showing only the XRD patterns of the sample DG-25. As the intensity of these additional peaks in our samples increased with the increase of $NaBH_4$ content in the TiO_2-$NaBH_4$ mixtures utilized for thermal annealing, it is clear that these peaks correspond to Ti_4O_5 and the brookite phase. The appearance of these new phases in the highly reduced samples probably due to the higher surface enthalpy of rutile than that of the anatase, which facilitates the reduction from rutile to TiO_{2-x}.[3]

From the XRD patterns, it was possible to determine the cell parameters for the anatase and rutile phases using the Bragg Law (equation 4.1), the following relationship:

$$\frac{1}{d^2} = \frac{h^2+k^2}{a^2} + \frac{l^2}{c^2} \qquad (4.1),$$

where:

- d is the interpaner distance
- a and c are the cell parameters in a tetragonal crystallographic system
- h, k, l are the Miller indices

The cell parameters of the unreduced and reduced nanoparticles were obtained taking into account the higher intensity peaks; i.e., (101), (004) and (200) peaks for anatase, and (110), (101) y (111) peaks for rutile. Once the cell parameters were obtained, they were used to estimate the unit cell volume and the density of the samples. Estimated values of these structural parameters of the samples are presented in Table 4.1. As can be seen, there is a small decrease in cell and structural parameters with the increase of $NaBH_4$ amount. It is in agreement with the fact that all the peaks in the XRD patterns are shifted to higher 2θ angles

with the increase in $NaBH_4$ amount, which also indicates a reduction in interplanar spacing, and the same for the cell parameters.

The average crystallite (grain) size, D, of the nanostructures was estimated using the Scherrer equation*:*

$$D = \frac{K\lambda}{\beta \cos \theta} \quad (4.2),$$

where

- D is the mean size of the crystallites,
- K is a dimensionless shape factor, which is generally 0.9 or 1, depending on the shape of the crystallites,
- λ is the X-ray wavelength,
- β is the line broadening at the half maximum intensity (FWHM),
- θ is the Bragg angle.

Since the TiO_2 nanoparticles of Degussa P25 consist of both anatase and rutile phases, the mean grain size of the unreduced and reduced nanoparticles were obtained by taking into account the peaks with higher intensities: (101), (004) and (200) for anatase, and (110), (101) y (111) for rutile. The estimated mean crystallite sizes of the samples are presented in Table 4.1. In general, the mean grain size in the samples decreased with the increase of $NaBH_4$, which is the result of a higher peak broadening at the half maximum caused by the reduction treatment. However, the grains of rutile phase suffered a higher decrease in size than the grains of anatase phase, which can be explained through the appearance of new phases. The weighted average grain size was estimated considering the mixed phase of the samples, whose proportions of anatase and rutile are 70% and 30%, respectively.

Structural parameter	DG-0		DG-10		DG-15		DG-25	
	Anatase	Rutile	Anatase	Rutile	Anatase	Rutile	Anatase	Rutile
a (nm)	$0.3685 \pm 2 \times 10^{-4}$	$0.4574 \pm 1 \times 10^{-4}$	$0.3683 \pm 6 \times 10^{-4}$	$0.4483 \pm 5 \times 10^{-4}$	$0.3686 \pm 7 \times 10^{-4}$	$0.4472 \pm 1 \times 10^{-3}$	$0.3667 \pm 1 \times 10^{-3}$	$0.4459 \pm 4 \times 10^{-4}$
c (nm)	$0.9486 \pm 3 \times 10^{-4}$	$0.2951 \pm 7 \times 10^{-4}$	$0.9268 \pm 7 \times 10^{-4}$	$0.2880 \pm 2 \times 10^{-4}$	$0.9264 \pm 7 \times 10^{-4}$	$0.2889 \pm 6 \times 10^{-4}$	$0.9231 \pm 5 \times 10^{-4}$	$0.2876 \pm 2 \times 10^{-4}$
Unit volumen cell (nm^3)	0.1288	0.0617	0.1257	0.0578	0.1258	0.0577	0.1241	0.0571
Density (kg/m^3)	4119.02	4298.37	4420.60	4588.41	4217.25	4596.36	4275.02	4644.66
Av. grain size (nm)	17.98	28.33	17.82	24.55	17.32	21.23	17.05	19.10
Weighted average grain size (nm)	21.08		19.75		18.49		17.66	
Microstrain	0.00507	0.00414	0.00473	0.00512	0.00473	0.00467	0.000846	0.007

Table 4.2. Estimated structural parameters for the anatase and rutile phases of the pristine and reduced TiO_2 nanoparticles.

It is well known that XRD peak broadening is associated to the grain size and microstrain, and they are connected with the relation:

$$\beta = \frac{\lambda}{D \cos\theta} + 4\varepsilon \tan\theta \qquad (4.3),$$

which is known as the Williamson and Hall (W-H) relation[4] and where:

- β is the peak broadening

- ϵ is the average internal microstrain

Equation (4.3) is a linear equation, and for multiple ordered diffraction patterns we can plot $\beta\cos\theta/\lambda$ against $4\sin\theta/\lambda$ (which will give a straight line). The inverse of intercept of this plot (W–H plot) will give the average crystallite size *D* and slope will give the average internal strain ε.

In Figure 3, we present the W-H plots for the unreduced and reduce TiO_2 nanoparticles, and the microstrain values estimated from the plots are listed in Table 4.1. We can observe that the results of the microstrain do not follow a regular trend with the increase of $NaBH_4$.

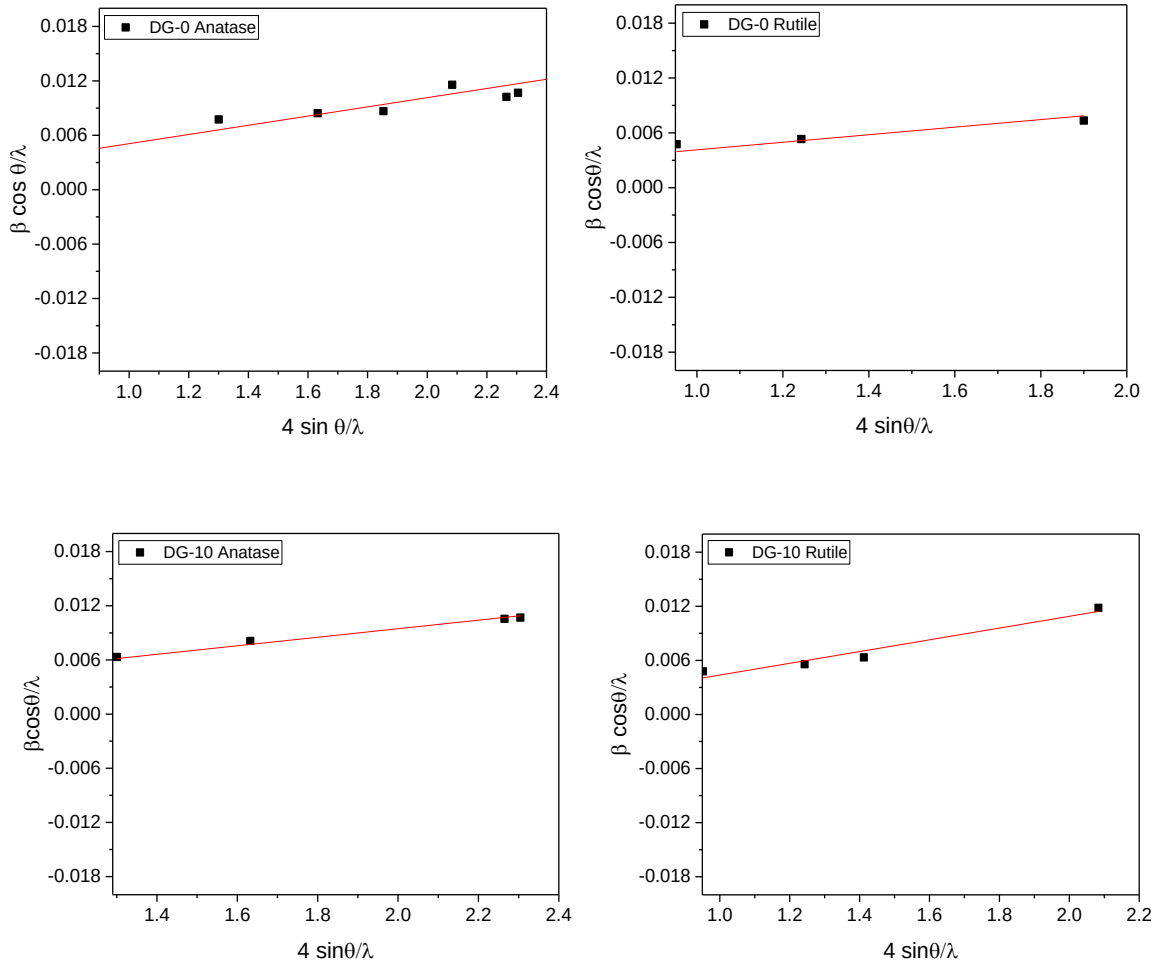

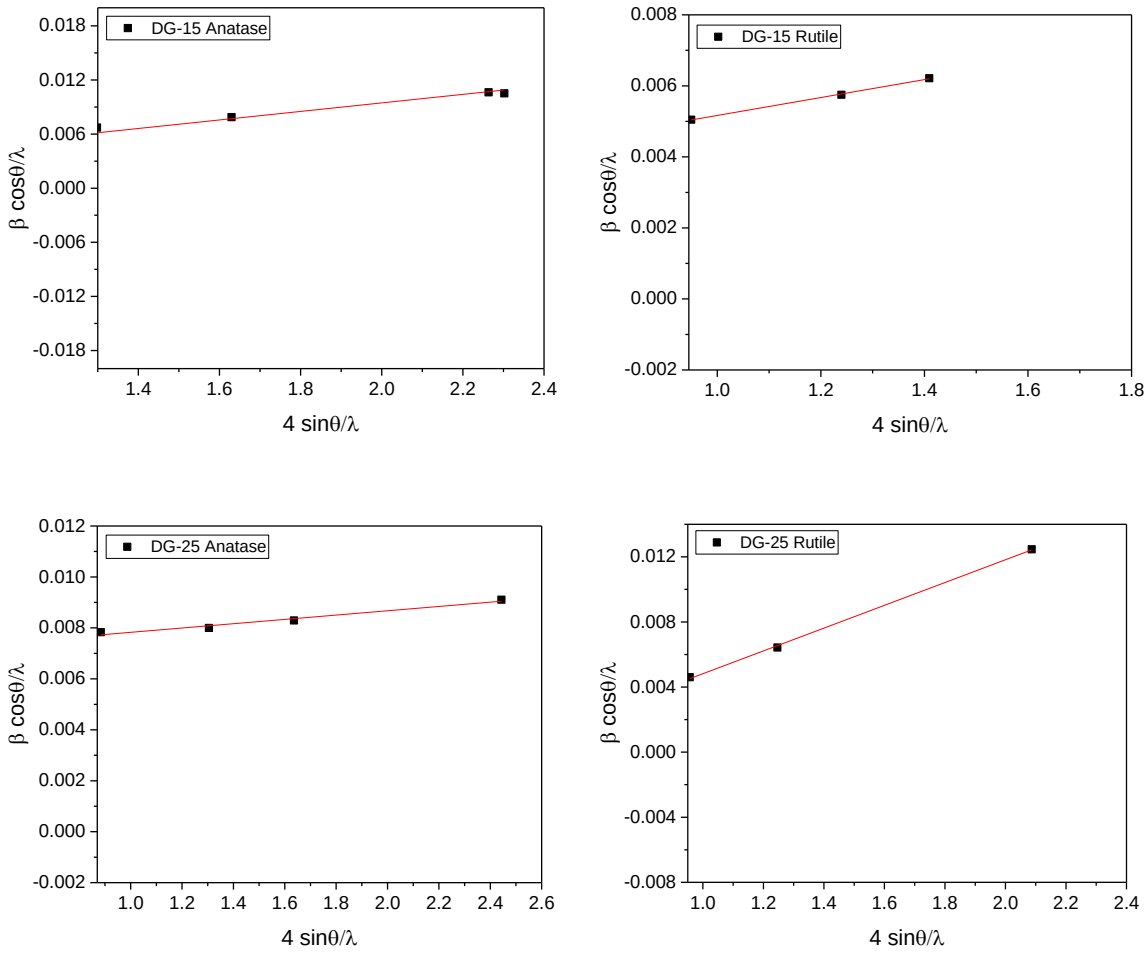

Figure 4.3. W-H plots of the unreduced and reduced TiO_2 nanoparticles for both phases (anatase and rutile).

Figure 4.4 shows some typical TEM micrographs of the prepared samples. As can be observed, all the four samples consist of small, well-defined and near-spherical shaped particles of 5-40 nm range. In order to estimate the average size of the nanoparticles, size distribution histograms were prepared by measuring the size of individual particles from the TEM micrographs of the samples. From the size distribution histograms (Figure 4.4), the average sizes of the particles in samples DG-0, DG-10, DG-15 and DG-25 were estimated to be 21.97, 22.18, 20.90 and 21.32 nm, respectively, which are in good agreement with the average crystallite size of the samples, estimated from their XRD analysis (Table 4.1).

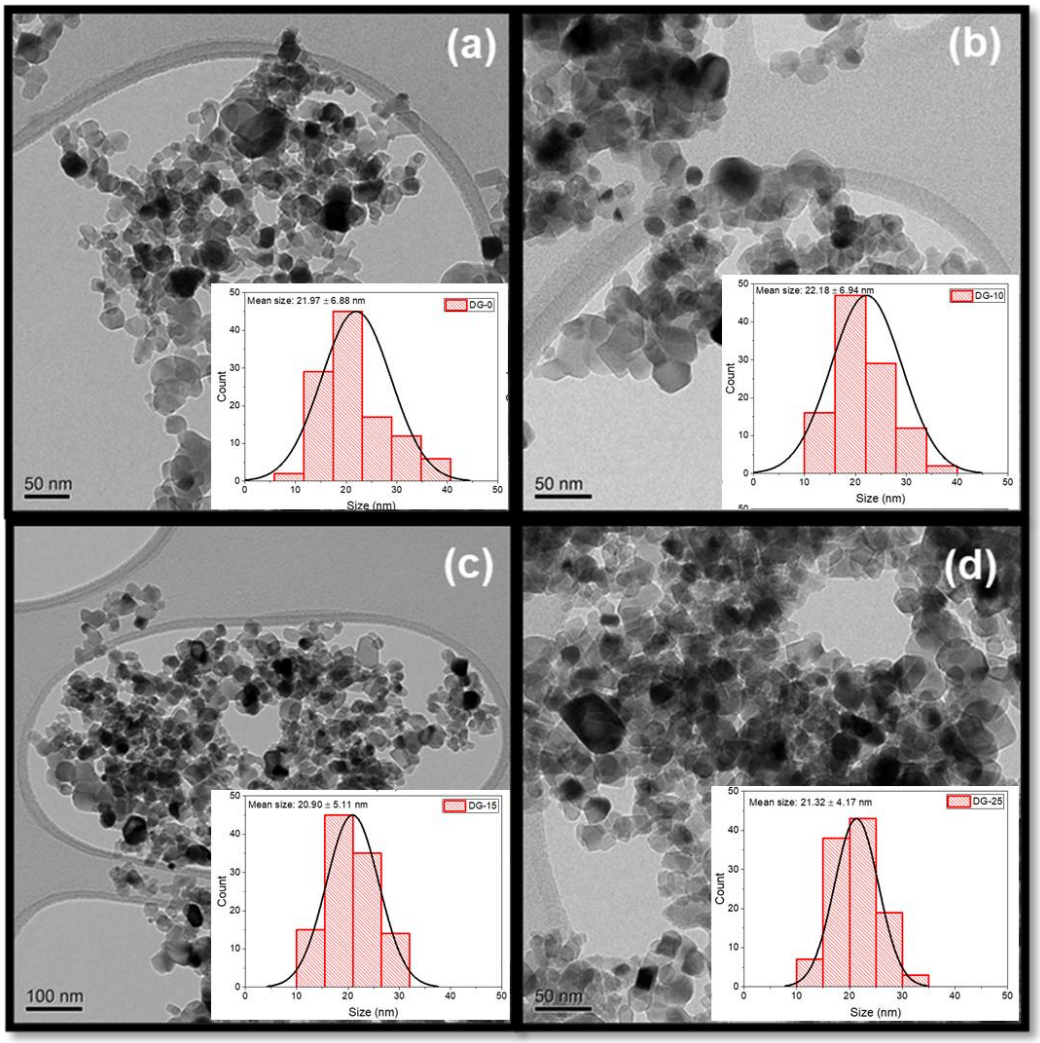

Figure 4.4. Typical TEM micrographs and their respective size distribution histogram of the TiO_2 nanoparticles with different amounts of $NaBH_4$: (a) 0, (b) 10, (c) 15 and (d) 25 wt%.

A careful analysis of the particle size values estimated from TEM analysis and the average grain size values estimated from the XRD analysis of the samples indicates the applied $NaBH_4$ reduction process does not have any significant effect on the average size of the nanoparticles, although it reduces the average grain size to some extent (Table 4.1). Such a reduction of average grain size due to the $NaBH_4$ reduction process indicate a reduction of crystallinity or formation of amorphous and disordered shell, especially in the samples prepared with higher amounts of $NaBH_4$, as can be seen in the HRTEM micrograph presented

in Figure 4.5. However, as can be seen in Figure 4.4, $NaBH_4$ reduction process does not have significant effect on the morphology of the nanoparticles.

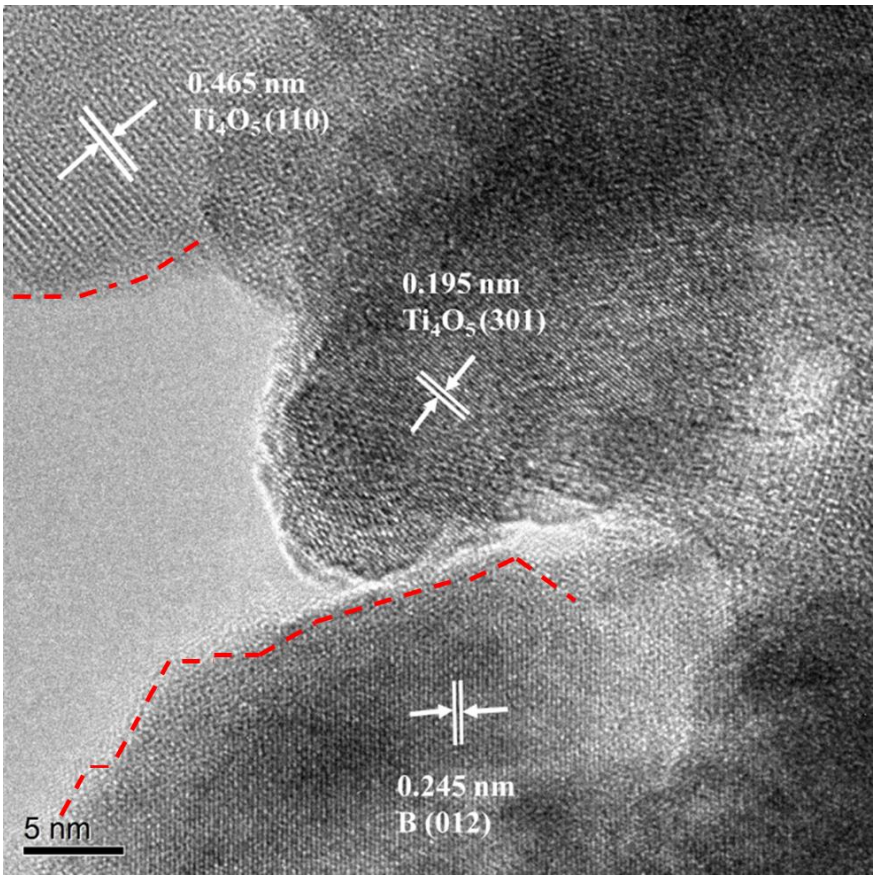

Figure 4.5. HRTEM micrograph of the sample prepared with the highest wt % of $NaBH_4$. The red dashed lines indicate the boundary of the amorphous and disordered region.

In order to study the optical properties of the pristine and the reduced TiO_2 nanoparticles, diffuse reflectance spectroscopy (DRS) was carried out. The DRS spectra of the samples recorded at room temperature are shown in Figure 4.6. As can be observed, all the samples revealed sharp absorption edges around 350 nm. In addition, absorbance of the samples in the visible spectral range increased with the increment of $NaBH_4$ content in the TiO_2 + $NaBH_4$ mixture. Since, the DRS spectra were recorder using pressed powder samples over the sample holder, and the pressed samples were about 5 mm thick, we can consider that the pressed samples have almost null transmittance in the UV-vis spectral range. According to

this, the relation A=1-R, where A is the absorbance and R the reflectance, was utilized to derive the reflectance spectra of the samples (from their absorbance spectra). In order to estimate the bandgap energy of the samples, the Kubelka-Munk[5] formalism was applied to the previously obtained reflectance spectra. Considering that the coefficient $F(R_\infty)$ in equation 3.5 of the previous chapter (chapter 3) is equivalent to absorbance, it was possible to plot $[F(R_\infty)h\nu]^{1/2}$ against the photon energy, $h\nu$, to obtain the bandgap, E_g of each of the samples, from the intersection of the linear fit to the photon energy axis (Figure 4.7).

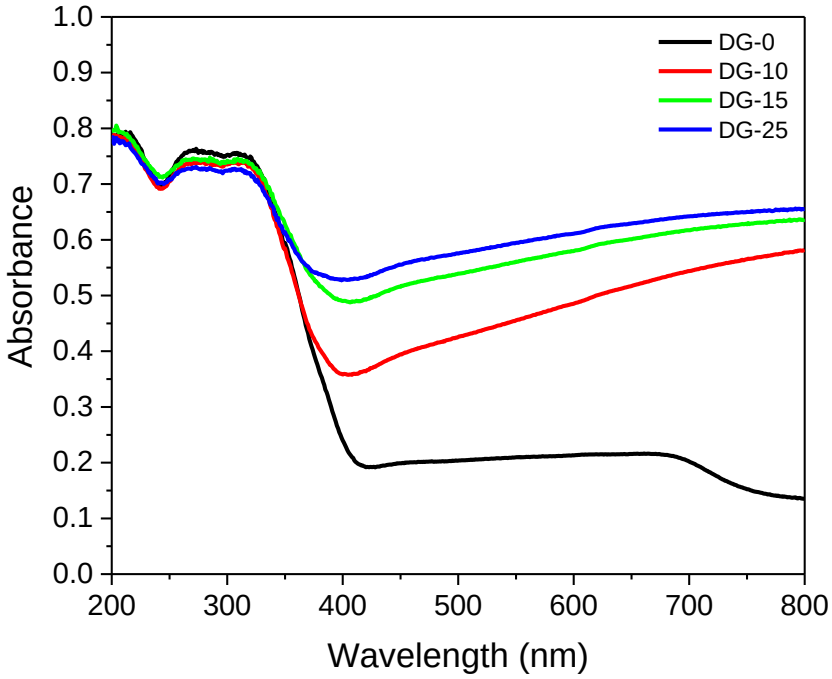

Figure 4.6. Absorption spectra of the pristine and the reduced TiO_2 nanoparticles.

Figure 4.7 shows the K-M plots utilized to estimate the bandgap energy of the samples, considering their indirect electronic transition. The bandgap energies estimated from the DRS analysis were 3.06, 3.03, 2.84 and 2.81 eV for the samples DG-0, DG-10, DG-15 and DG-25, respectively. We can observe a reduction in the bandgap energy of the TiO_2 nanoparticles with the increase of oxygen vacancies on their surface (due to $NaBH_4$-assisted reduction).

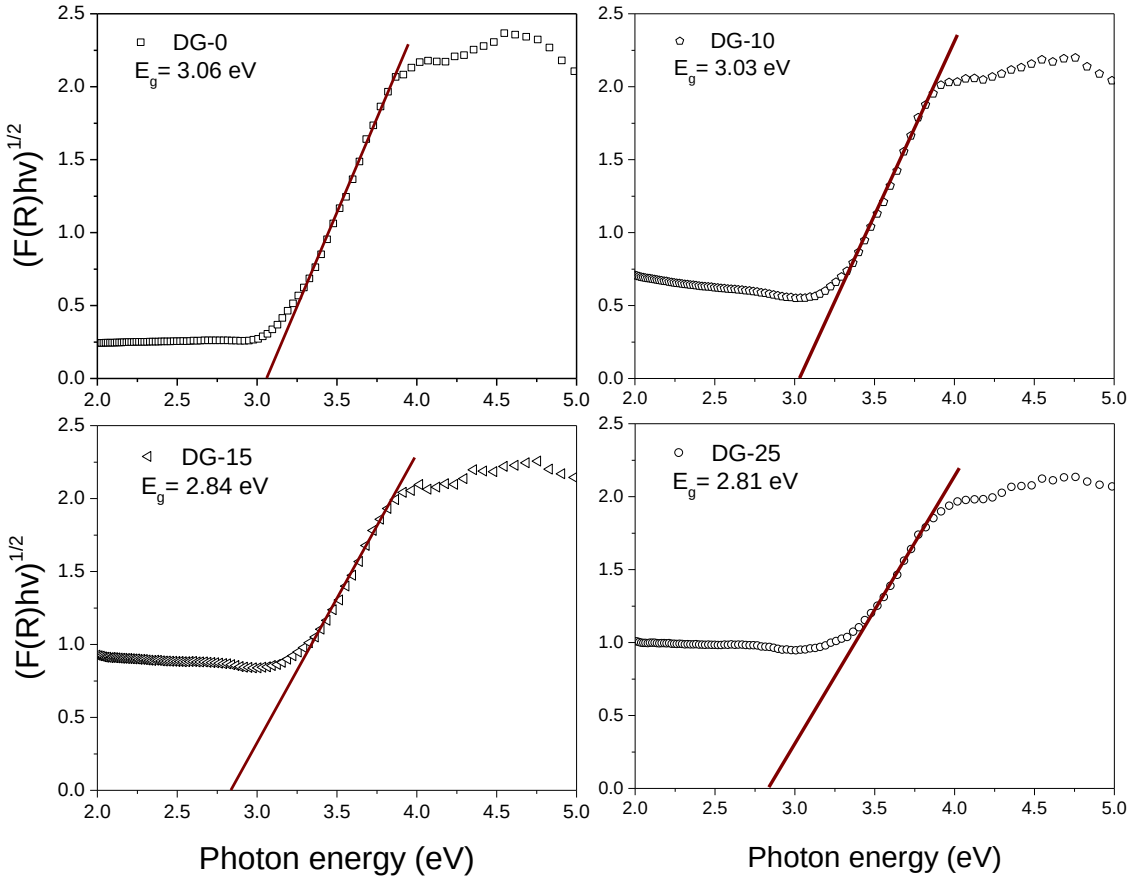

Figure 4.7. Kubelka-Munk treated reflectance spectra for unreduced and reduced TiO_2 nanoparticles utilized for estimating their bandgap energies.

Raman spectra of pristine and reduced TiO_2 nanoparticles recorded at room temperature are presented in Figure 4.8. As can be observed, there appeared several Raman bands with well-defined peak positions and of high intensities in the samples, indicating their good crystallinity. The typical Raman-active vibrational modes appeared at around 142.5 (E_g), 195.1 (E_g), 395.3 (B_{1g}), 514.9 (A_{1g}) and 637.8 cm^{-1} (E_g) correspond to the anatase phase are marked with black dashed lines. On the other hand, the Raman-active vibrational modes appeared around 447 (E_g) and 609 cm^{-1} (A_{1g}) corresponding to the rutile phase are marked with orange dashed lines.[3]

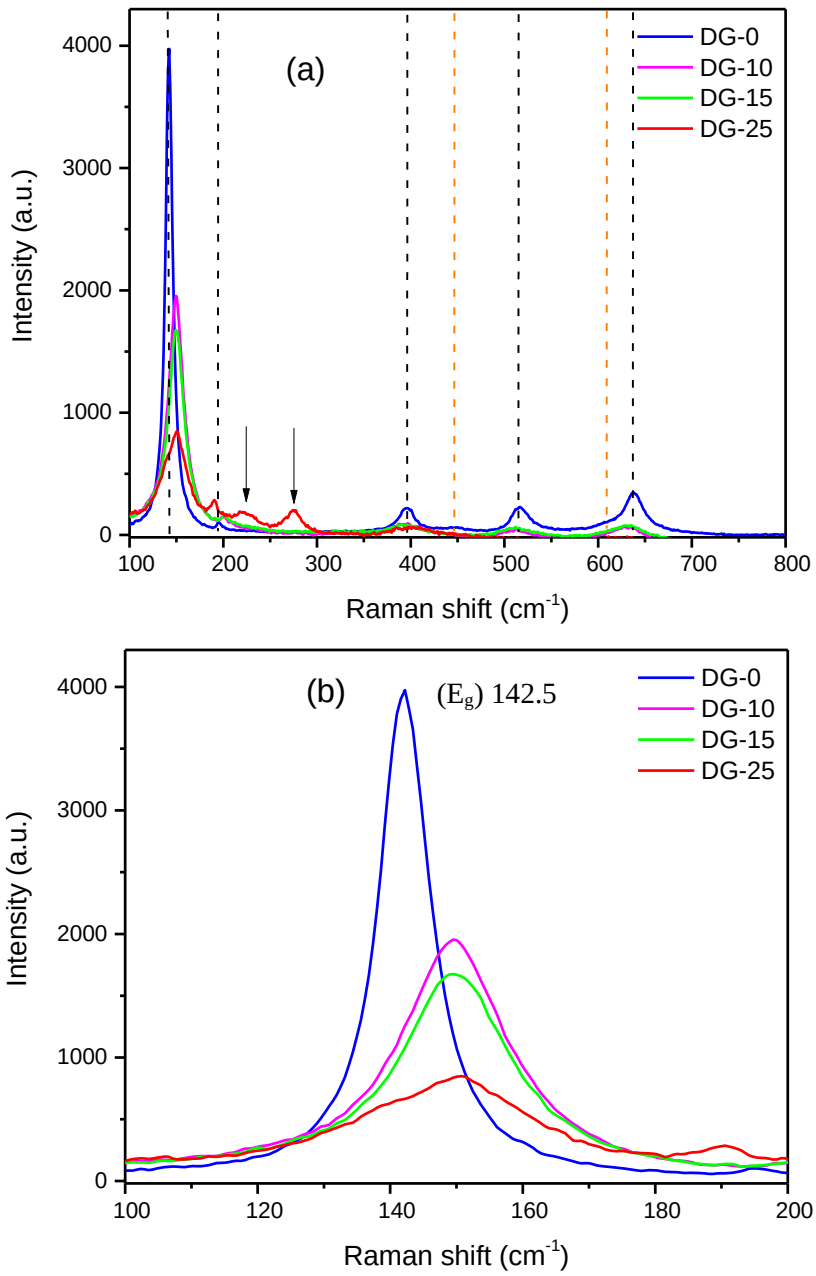

Figure 4.8. (a) Raman spectra of the unreduced and reduced TiO_2 nanoparticles; (b) Principal Raman bands of the TiO_2 (reduced and unreduced) nanostructures in amplified energy scale to show their intensity and FWHM variations with the increase of $NaBH_4$ in the reaction mixture.

The strongest mode, E_g, is assigned to the stretching vibration of the Ti-O bond. We can observe that, with the increase of the reducing agent, the position of the principal Raman band (with highest intensity) appeared around 142.5 cm^{-1} shifted towards higher

wavenumber, and the intensity decreased severely. This reduction in the scattering intensity as well as the blue-shift of the E_g mode (142.5 cm^{-1}) can be due to a breakdown of long-range translational symmetry in the crystallites caused by the generation of oxygen vacancies at the surface of the TiO_2 nanoparticles due to borohydride reduction.[6] It could be also noticed a gradual broadening of the Raman bands with the increase of $NaBH_4$ in the reaction mixture, which is due to the increase of oxygen vacancies. Moreover, two new peaks appeared (marked with black arrows) around 219.6 and 275.6 cm^{-1} in the sample DG-25, which could be tentatively assigned to the vibrational modes B_{1g} and B_{3g}, respectively, of the TiO_2 in the brookite phase.[7] As can be remembered, we also detected the XRD peaks correspond to the brookite phase in the XRD pattern of the DG-25 sample. So, the Raman results of the samples are in good agreement with their XRD results.

To understand the effect of reductor ($NaBH_4$) concentration on the texture parameters of the nanostructures, we measured their N_2 adsorption-desorption isotherms (Figure 4.9). As we can see in Figure 4.9, all the samples revealed typical type II isotherms with sharp adsorptions at very low and very high relative pressures, suggesting the presence of nonporous or microporous adsorbent surface. The gradual curvature of the isotherm is an indication of a significant amount of overlap of monolayer coverage and the onset of multilayer adsorption.[8]

Table 4.2 compiles the BET surface area, total pore volume and average pore diameter for the pristine and reduced TiO_2 nanoparicles. It can be seen that in general, the BET surface area of the TiO_2 nanoparticles does not follow a regular trend with the reduction treatment with $NaBH_4$. However, in the sample DG-15 the total pure volume slightly increased, which could be beneficial for their heterogeneous photocatalytic applications, as a higher pore volume may enhance the capture capacity of the organic pollutants intended to be degraded by the catalyst. As can be noticed in Table 4.2, the variation of pore volume or average pore size in the nanoparticles due to the variation of reductor concentration is not so significant, and they do not follow a particular trend. Average pore diameter (size) in the samples varied in-between 39 and 49 nm, indicating their mesoporous nature.

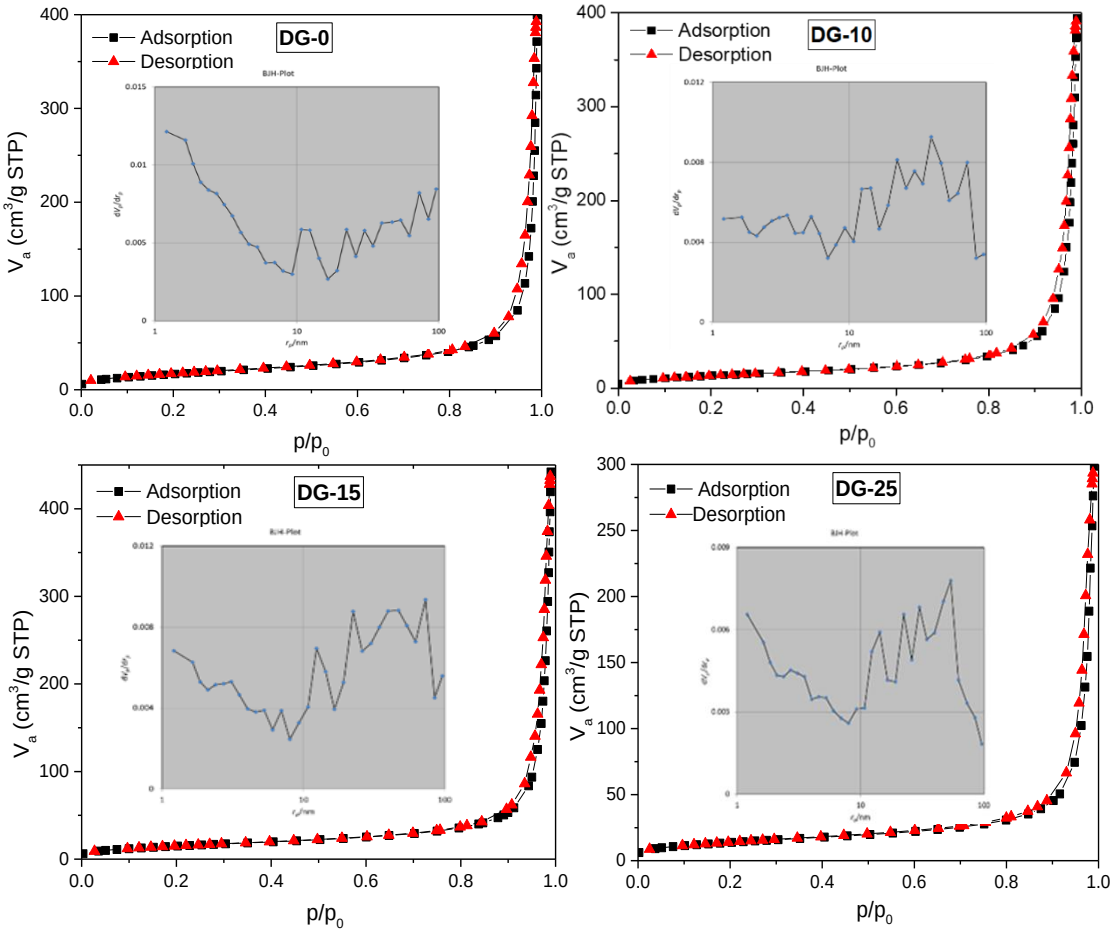

Figure 4.9. N_2 adsorption-desorption isotherms of the pristine (unreduced) and the reduced TiO_2 nanoparticles. Insets show the pore size distribution of corresponding sample.

Sample	BET Surface area (m^2/g)	Total pore volume (cm^3/g)	Average pore diameter (nm)
DG-0	62.46	0.62	39.47
DG-10	49.19	0.60	49.11
DG-15	54.92	0.68	49.40
DG-25	49.27	0.45	36.94

Table 4.3. Textural parameters of the unreduced and the reduced TiO_2 nanoparticles estimated from their N_2 adsorption-desorption isotherms recorded at 77K.

Figure 4.10 shows the Z-potential vs the amount of $NaBH_4$ used to prepare the reduced TiO_2 nanoparticles. Since results of measurements of Z-potential of TiO_2 nanoparticles in aqueous suspensions can be affected by several factors, such as pH, the aqueous solutions/suspensions were prepared controlling and setting a pH of 7.1, approximately, for all the samples. The Z-potential decreased as the amount of $NaBH_4$ increased, obtaining -17.9, -32.8, -35.4 and -37.2 mV for DG-0, DG-10, DG-15 and DG-25, respectively. These results mean that, due to the generation of oxygen vacancies on the TiO_2 nanoparticles surface, a change in their surface electronic charge and surface energy are altered, resulting in higher adsorption and affinity of protons on their surface.[9]

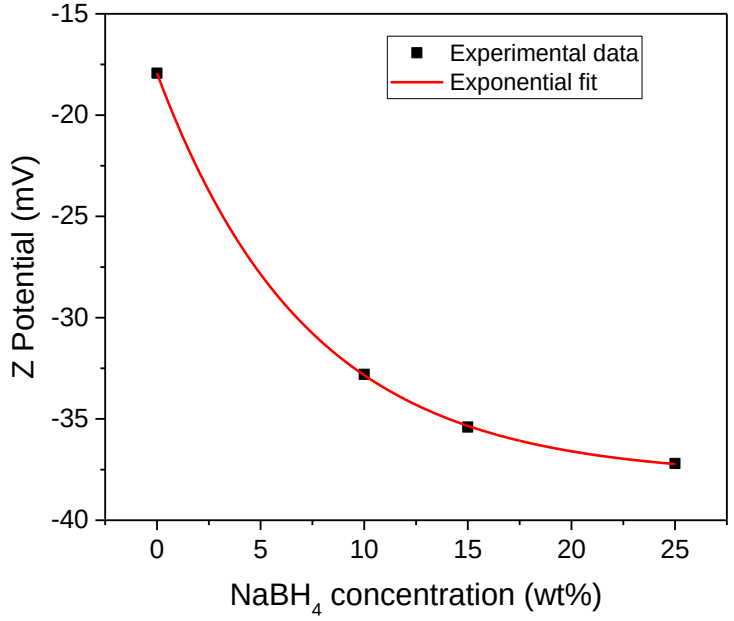

Figure 4.10. Z potential of TiO_2 nanoparticles prepared with different amounts of $NaBH_4$.

The photocatalytic activity of the TiO_2 nanoparticles was evaluated in the photodegradation of methylene blue (MB). The experiments were carried out using 30 mg of photocatalyst (pristine and reduced TiO_2 nanoparticles) in 60 mL of 10 ppm methylene blue aqueous solution. In order to study the concentration of methylene blue in the photodecomposition process, a calibration curve of this organic dye was prepared by measuring the absorption

spectra of aqueous MB solutions of 3, 5, 10, 20 y 25 ppm concentrations. The maximum of the principal absorption band of MB (664 nm) was considered for preparing the calibration curve (Figure 4.11). The resulting calibration curve shown in Figure 4.11 was used to estimate the concentration of MB in the aqueous solution in the photodecomposition process.

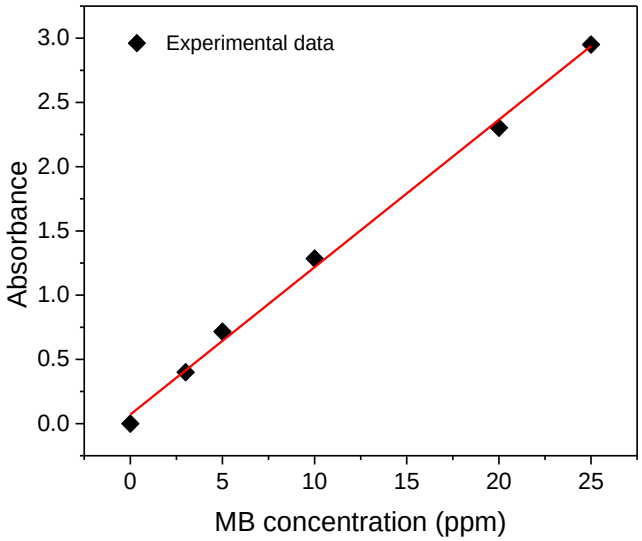

Figure 4.11. Calibration curve of methylene blue.

The temporal evolution of the absorption spectra of methylene blue before and during the photodegradation process using unreduced and reduced TiO_2 nanoparticles are shown in Figure 4.12. In this figure, (a) corresponds to the adsorption-desorption process for the corresponding sample, which occurred in the dark. There is a small and gradual decrease in the intensity of the absorption band (664 nm) of methylene blue in DG-0. However, for the samples DG-10, DG-15 and DG-25 the decrease in the peak intensity occurs in a very drastic manner, due to the high adsorption of methylene blue molecules at the surface of the nanoparticles. We can notice that the decrease in intensity is almost proportional to the wt % of $NaBH_4$ utilized for the preparation of the nanostructures. This is in good agreement with the results of the Z-potential study, where we found that more negative the z potential at the surface of a nanoparticle, higher is its affinity to protons. Since MB is a cationic dye, it can be easily adsorbed and accumulated at the negative charged surface of the nanoparticles. On

the other hand, for all the samples, (b) represents the absorption spectra of the MB solution during their photocatalytic degradation by the TiO_2 (unreduced and reduced) catalysts under UV irradiation. As can be seen, the higher the concentration of $NaBH_4$ is, the lower is the degradation rate, i.e., the intensity of the MB absorption band changes in slower rate. This occurs because, due to high adsorption of MB molecules, the surface of the reduced TiO_2 nanoparticles become partially or fully covered, which inhibits the light absorption, and consequently, the photodegradation process.

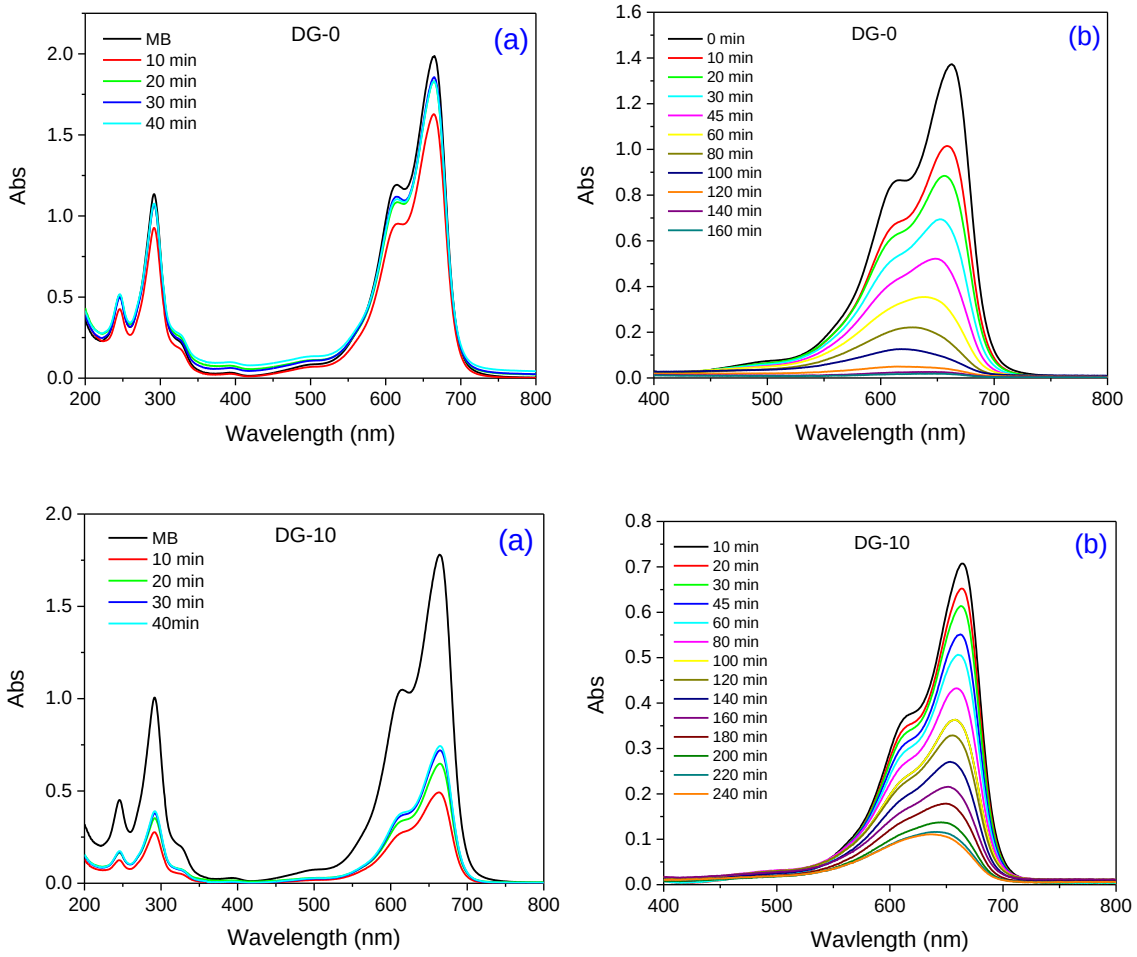

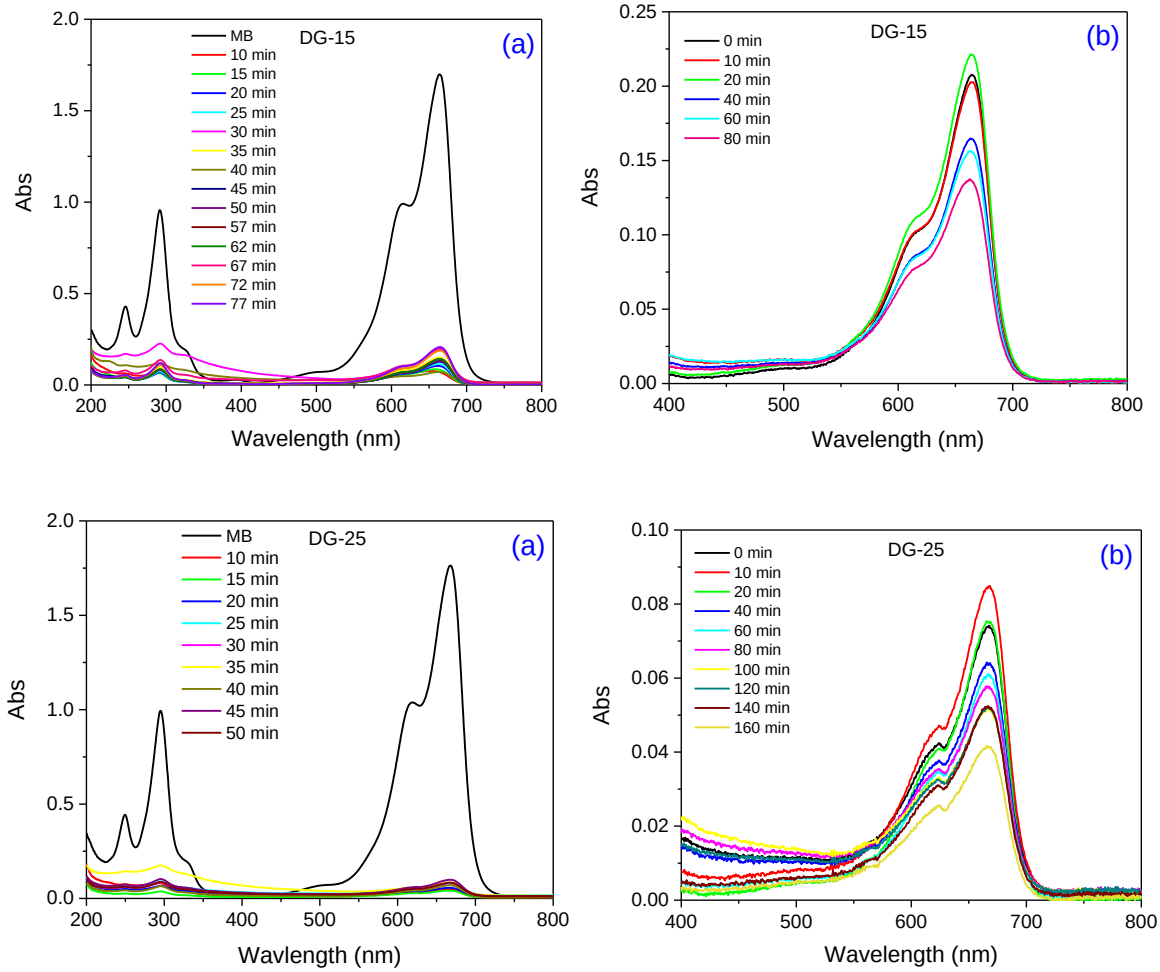

Figure 4.12. (a) Absorption spectra of MB solution in presence of unreduced and reduced TiO_2 nanoparticles in the dark. (b) Absorption spectra of MB solution in presence of reduced TiO_2 nanoparticles under UV light.

For evaluating the photocatalytic activity of the TiO_2 samples, the change in relative concentration (C/C_0) of MB molecules in the reaction mixture with reaction time after illuminating the reaction mixture with UV light. With the degradation of MB, there occurs a gradual decolorization of the reaction solution, and a gradual intensity reduction of the principal absorption band in the absorption spectra of the dye solution.

The photocatalytic activities of the pristine and the reduced TiO_2 nanoparticles were tested in the photodegradation of MB under UV light, and the results are shown if Figure 4.13. From these results, it is noticeable that the photocatalytic activity of the unreduced TiO_2

nanoparticles is higher than that of the reduced TiO_2 nanoparticles under UV radiation. It can also be seen that the photocatalytic activity of the samples DG-0 and DG-10 show a similar behavior during all the photodecomposition process, 10 min after the moment in which the UV light was on. However, the samples DG-15 and DG-25 show a drastic decrease in the relative concentration and it can be seen that the photodecomposition of MB does not occur under UV light, because most of the dye molecules have been adsorbed on the surface of the nanoparticles, limiting both the light absorption and the quantity of dye molecules to be photodegraded.

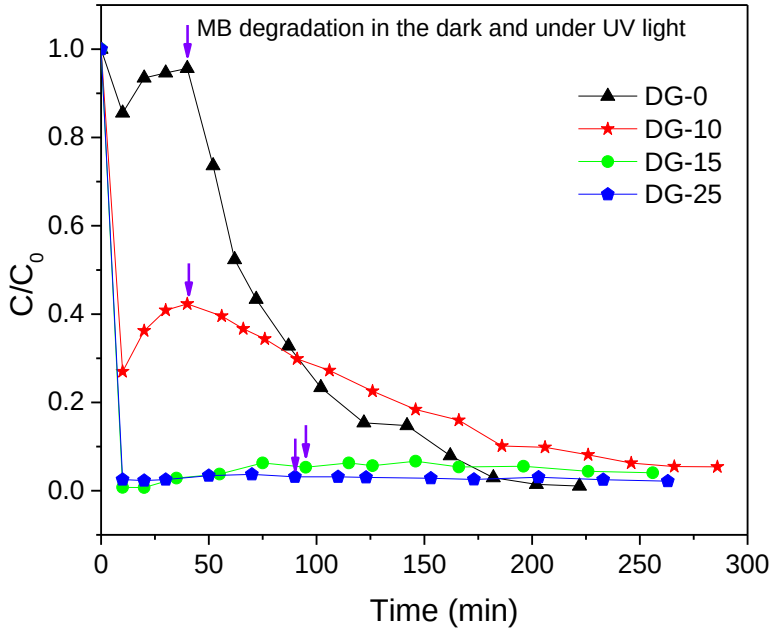

Figure 4.13. Kinetics of MB photodegradation by TiO_2 nanoparticles prepared with different amounts of $NaBH_4$ under UV illumination. The purple arrows represent the moment in which the stabilization of adsorption-desorption occurred, so the UV lamp was lit.

As can be observed in figure 4.13, the reduced particles have a high MB absorption capacity. Within 50 minutes of addition of these nanoparticles, a great fraction (> 50%) of the MB molecules present in the reaction mixture get adsorbed over TiO_2 nanoparticles separating from the reaction mixture. Also, the extent of MB adsorption at the surface of TiO_2 nanoparticles increases with the increase of $NaBH_4$ reductor utilized for their reduction; in

other words, with the extent of reduction of the particles. For the same reason, the degradation rate of MB occurs very slowly after the irradiation of UV light.

The kinetics of the MB degradation was evaluated using the Langmuir-Hinshelwood (L-H) model, which describes a pseudo first-order kinetics, where the initial concentration of the solution affects the photocatalytic degradation rate of the organic compounds.[10] At low initial dye concentration, the rates of photodegradation of MB can be given by:

$$\ln C = -kt + \ln C_0 \qquad (4.4).$$

Equation (4.5) has the form of a linear equation where k is the constant (in min^{-1}) of the pseudo first-order rate, which can be written as:

$$\ln(C_0/C) = kt \qquad (4.5).$$

A plot of $\ln(C_0/C)$ versus UV irradiation time for the MB photodegradation by the reduced TiO_2 nanoparticles is shown in Figure 4.14. The values of k were obtained from the linear fits of the plot of Figure 4.14. We can observe from this figure that the highest value of k corresponds to the sample DG-0, which means that these unreduced TiO_2 nanoparticles have a better photocatalytic activity than the reduced TiO_2 nanoparticles.

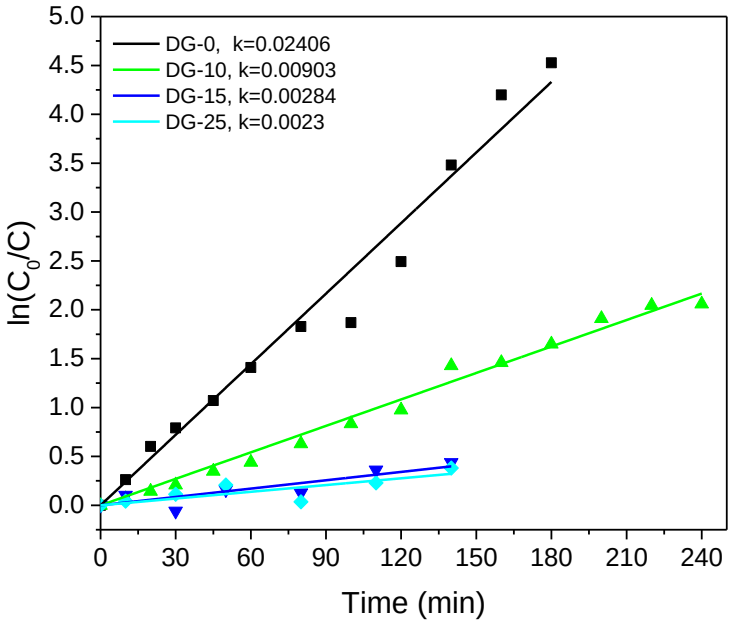

Figure 4.14. Kinetic fits for the photocatalytic degradation of MB by the unreduced and reduced TiO_2 nanoparticles.

As the utilized $NaBH_4$ reduction reduces the bandgap energy of the TiO_2 nanoparticles (see in the section 2.5.5), we also evaluated their photocatalytic performance in the degradation of MB under visible light. For this, we followed the same experimental process as in the case of UV irradiation, keeping all the experimental conditions same except the irradiation. In the present case, we utilized a visible light (from a 10 W xenon lamp) for irradiating the reaction mixture. The results of the decolorization of MB under visible light are shown if Figure 4.15. The results show a similar behavior to the one obtained for the photocatalytic evaluation under UV light, being DG-0 the sample which shows a better photocatalytic behavior. In fact, in the present case also, the reduced photocatalysts adsorbed more than 50% MB molecules within 50 min of their incorporation in the reaction mixture, even under dark (without illumination).

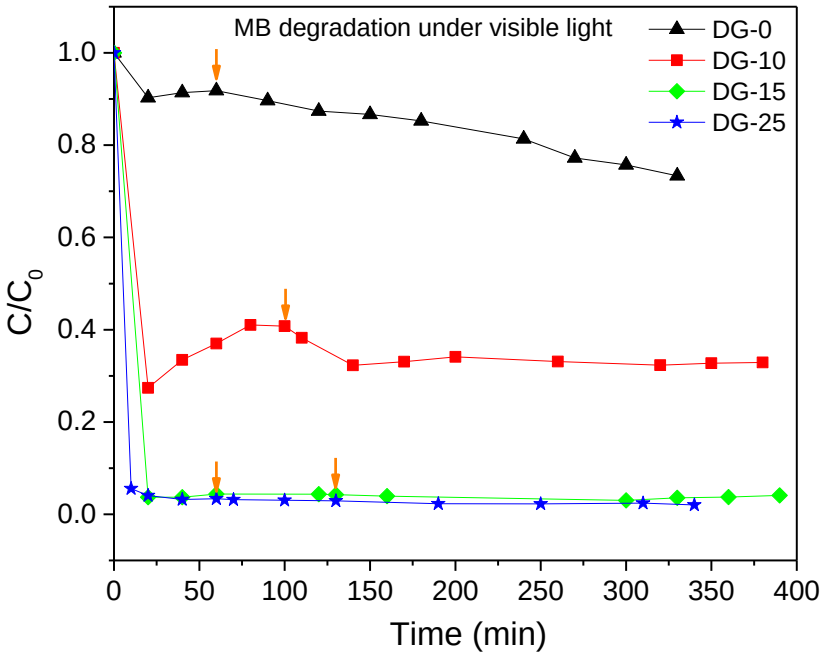

Figure 4.15. Kinetics of MB photodegradation by TiO_2 nanoparticles prepared with different amounts of $NaBH_4$ under visible light. The orange arrows represent the moment in which the stabilization of adsorption-desorption occurred, so the visible lamp was lit.

From the results obtained in the visible light induced photocatalytic activity evaluation, it is clear that the amounts of $NaBH_4$ used in the reduction treatment led to the formation of TiO_2 nanoparticles working better as adsorbent materials rather than photocatalytic materials. For this reason, we decided to prepare two extra samples using 2 and 5 wt % of $NaBH_4$, labeled as DG-2 and DG-5, respectively. These samples were characterized by the BET and Z-potential techniques, in order to understand better the adsorption-desorption process and its effect in the photocatalytic performance.

The N_2 adsorption-desorption isotherms of the samples DG-2 and DG-5 are shown in Figure 4.16. It can be noticed that the results are very similar to the ones obtained for the samples prepared earlier (samples DG-19, DG-15 & DG-20), revealing type II isotherms. In Table 4.3, the estimated textural parameters of the samples, such as BET surface area, total pore volume and average pore diameter are summarized. As can be seen in Table 4.3, there is a slight increase in pore volume and pore diameter in DG-5. However, only the DG-2 sample showed a mesoporous nature, since its pore diameter is less than 50 nm.

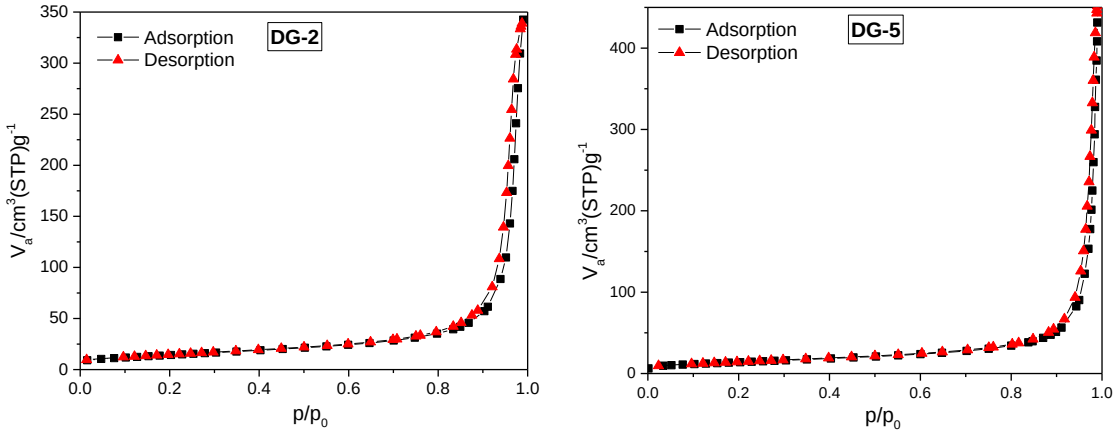

Figure 4.16. N_2 adsorption-desorption isotherms of the DG-2 and DG-5 samples.

Sample	BET Surface area (m^2/g)	Total pore volume (cm^3/g)	Average pore diameter (nm)
DG-2	51.53	0.53	40.94
DG-5	50.29	0.67	53.61

Table 4.4. Texture parameters of the reduced TiO_2 nanoparticles estimated from their N_2 adsorption-desorption isotherms recorded at 77K.

The results of Z-potential measurement of the samples DG-2 and DG-5 at pH ~ 7.1 are compiled with the Z-potentials of rest of the samples, and presented graphically in Figure 4.17. Estimated Z- potential values for the samples DG-2 and DG-5 were -21.5 and -26.1 mV, respectively. The results follow the trend observed for the other samples, that is to say, the Z-potential decreases with the increase of $NaBH_4$ amount utilized in the reduction process of the TiO_2 nanoparticles.

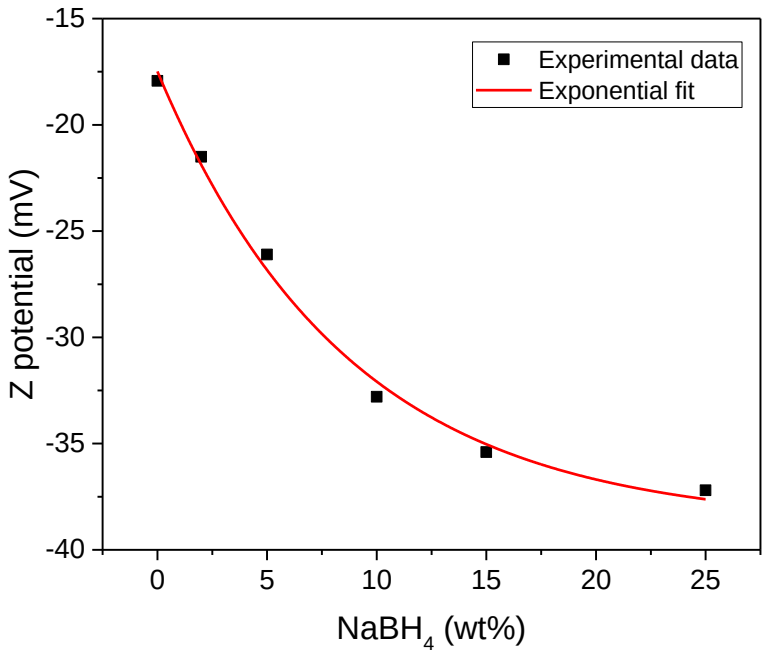

Figure 4.17. Z-potential of the reduced TiO_2 nanoparticles prepared with different amounts of $NaBH_4$.

Finally, the results of the photocatalytic evaluation under UV and visible light of the DG-2 and DG-5 samples together with that of the other samples (DG-0, DG-10, DG-15 and DG-25) are presented in Figure 4.18. The samples DG-2 and DG-5 showed higher photocatalytic activity than DG-10, DG-15 and DG-25 samples. However, for both the samples, adsorption of MB (at the surface of the NPs) is higher than that of the sample DG-0. Both the samples (DG-2 & DG-5) show a higher photodegradation rate of MB under UV irradiation than the DG-10, DG-15 and DG-25 samples, although the efficiency of MB degradation of these two samples remained inferior to that of the sample DG-0, i.e., the TiO_2 NPs with minimum oxygen vacancies (V_O) at their surface. From the obtained photocatalytic results, it is clear that the reduced TiO_2 nanoparticles prepared in this investigation are good adsorbents for MB molecules due to their high negative Z-potential. However, their high adsorption capacity affects their photocatalytic activity adversely. Using equation (4.5) the reaction constants k of the two newly prepared samples, i.e., DG-2 and DG-5 for MB photodegradation were calculated to be 0.01083 and 0.00791, respectively. These values indicate the sample DG-2 has faster photocatalytic degradation rate for MB than that of the

sample DG-5 under UV illumination. However, the photocatalytic performance of the sample DG-2 is still inferior to the photocatalytic performance of the sample DG-0.

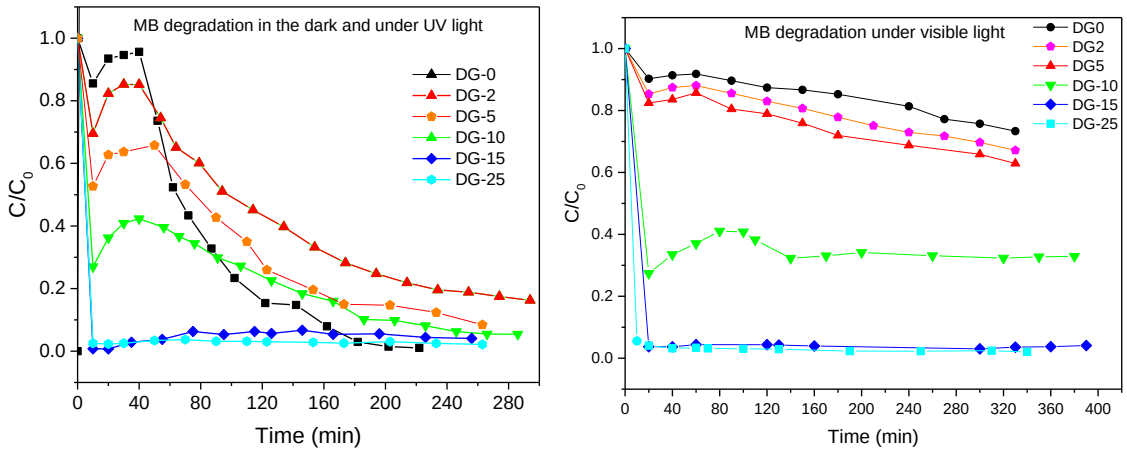

Figure 4.18. Kinetics of MB photodegradation by TiO_2 nanoparticles prepared with different amounts of $NaBH_4$ under UV illumination (left) and under visible light (right).

Although we were expecting a higher photocatalytic activity of the reduced TiO_2 NPs, the results obtained in this research by testing them in the photodegradation of methylene blue (a model dye) indicate that $NaBH_4$ reduction of TiO_2 NPs creates oxygen vacancies in high concentration at their surface, and modify the Z-potential of their surfaces. The high and negative Z-potential of the reduced TiO_2 NPs make them efficient adsorbers for capturing cationic dye molecules. Further research is required for optimizing the V_O concentration at the surface of the reduced TiO_2 NPs, i.e., the amount of $NaBH_4$ in the reaction mixture for their reduction, for effective application of the metal oxide nanoparticles in organic dye degradation under UV and Visible light. On the other hand, it could be also useful to test the photocatalytic activity of the reduced TiO_2 nanoparticles on the dyes with a different (i.e., anionic and non-ionic) ionic natures.

References

1. Sorcar, S., Hwang, Y., Grimes, C. A. Highly enhanced and stable activity of defect-induced titania nanoparticles for solar light-driven CO_2 reduction into CH_4. *Materials Today* 20**,** 507-515 (2017).

2. Ye, M., Jia, J., Wu, Z., Qian, C., Rong, C., O'Brien, P., Sun, W., Dong and Ozin, G. Synthesis of Black TiO_x Nanoparticles by Mg Reduction of TiO_2 Nanocrystals and their Application for Sola Water Evaporation. *Avanced Energy Materials* 1601811, (2016).

3. Hu, L., Li, Y., Zheng, W., Peng, Y., Tsang, S., Lee, L., Wong, K. Blue ordered/disordered Janus-type TiO_2 nanoparticles for enhanced photocatalytic hydrogen generation. *Journal of Materials Chemistry A* 8, 22828-22839 (2020).

4. G.K. Williamson, W.H. Hall, X-ray line broadening from filed aluminium and wolfram. *Acta Metallurgica* 1(1), 22-31 (1953).

5. Kubelka, P., and Munk, F. Ein Beitrag Zur Optik Der Farbanstriche. *Techn. Phys.,* 12, 593 -601 (1931).

6 Pal, M., Pal, U., Jiménez, J.M., Perez, F. Effects of crystallization and dopant concentration on the emission behavior of TiO_2: Eu nanophosphors. *Nanoscale Research Letters* 7, 1 (2012).

7. Tompsett, G.A., Bowmaker, G.A., Cooney, R.P., Metson, J.B., Rodgers, K.A. and Seakins, J.M. The Raman spectrum of brookite, TiO_2 (*Pbca, Z* = 8). J. *Raman Spectroscopy* 26: 57-62 (1995).

8. Thommes, M., Kaneko, K., Neimark, A., Olivier, J., Rodriguez, F., Rouquerol, J., Sing, K. Physisorption of gases, with special reference to the evaluation of surface area and pore size distribution (IUPAC Technical Report). *Pure and Applied Chemistry* (2015).

9. Liao, D., Wu, G., Liao, B. Zeta potential of shape-controlled TiO_2 nanoparticles with surfactants. *Colloids and Surfaces A: Physicochemical and Engineering Aspects* 348, 270-275 (2009).

10. Morales, N., Pal, U., Galeazzi, R., Sandoval, A. Effects of morphology, surface area, and defect content on the photocatalytic dye degradation performance of ZnO nanostructures. *Royal Society of Chemistry Advances* 4, 41099 (2014).

Conclusions

From the results obtained in this investigation, we can draw the following conclusions:

- Post-treatment process utilizing $NaBH_4$ as a reducing agent is an efficient method for synthesizing reduced TiO_2 nanoparticles, controlling (qualitatively) the amount of oxygen vacancies on their surfaces.
- The variation of oxygen vacancy in the nanostructures is manifested by gradual variation of color, from light blue to back.
- While the utilized amount of $NaBH_4$ does not affect the morphology or the initial size of the TiO_2 NPs, it affects their crystallinity, modifying the size of unit cell parameters and average crystallite size. Utilization of $NaBH_4$ more than 15 wt % induces the formation of brookite phase, along with the formation of an amorphous Ti_4O_5 phase at the surface of pristine TiO_2 NPs.
- Formation of V_O at the surface enhances the light absorption capacity of TiO_2 nanoparticles in the visible spectral range as a consequence of a significant narrowing of bandgap.
- The generation of oxygen vacancies at the surface reduced TiO_2 nanoparticles modifies the charge (negative) density at their surface, causing an enhancement of their adsorption capacity towards cationic dye molecules such as MB.
- While the objective of this work was to correlate the photocatalytic activity of TiO_2 nanoparticles to the concentration of oxygen vacancies qualitatively, the results obtained in this investigation indicate the reduced TiO_2 nanoparticles are highly adsorptive, especially to the Methylene blue (MB), which is a cationic dye.
- Due to the high adsorption of dye molecules on the surface and consequent blocking of incident radiation, the reduced TiO_2 nanoparticles do not manifest a high photocatalytic activity towards MB degradation under UV or visible radiation. Although a moderated adsorption of dye molecules at the surface of the catalyst is beneficial for their photodegradation, it seems for photocatalytic application, the NPs should have an optimum V_O concentration, which needs further investigation.